DEPARTMENT OF PHYSICS
UNIVERSITY OF JYVÄSKYLÄ
RESEARCH REPORT No. 11/2013

REAL-SPACE QUANTUM TRANSPORT IN TWO-DIMENSIONAL NANOSTRUCTURES IN MAGNETIC FIELDS

BY
VILLE KOTIMÄKI

Academic Dissertation
for the Degree of
Doctor of Philosophy

To be presented, by permission of the
Faculty of Mathematics and Natural Sciences
of the University of Jyväskylä,
for public examination in Auditorium FYS1 of the
University of Jyväskylä on November 29, 2013
at 12 o'clock noon

UNIVERSITY OF JYVÄSKYLÄ
Jyväskylä, Finland
November 2013

Preface

The work reviewed in this thesis has been carried out during the years from 2008 to 2013 at the Department of Physics and the Nanoscience Center of the University of Jyväskylä, Finland.

First I would like to thank my supervisor Prof. Esa Räsänen for his guidance and support during my PhD project. With your help I have become much more independent and the life hacks you have shared with the group have already proven to be very useful. Prof. Afif Siddiki, Dr. Aysevil Salman, Dr. Engin Cicek, Dr. Holger Hennig and Prof. Eric Heller are gratefully acknowledged for the fruitful collaboration that has enabled me to complete my thesis. I want to thank the past and present members of the Quantum Control and Dynamics group for the nice work atmosphere. I would also like to thank Prof. Päivi Törmä for accepting me into her group where I could test my skills on theoretical and experimental physics during my master's studies. I am grateful to Dr. Andreas Johansson for teaching me the basics of how to work in the field of experimental physics.

I want to thank the Department of Physics and the Nanoscience Center for providing an excellent place to work and study. I have been privileged to be a part of such a warm scientific community that really takes good care of its members. Special thanks go to the office personnel making sure that all mundane issues are solved without a fuss. I am also very grateful to the Department of Physics for allowing me to teach the younger students. It has been a great pleasure to work and study with the great lecturers of the Department of Physics: Prof. Robert van Leeuwen, Dr. Pekka Koskinen, Prof. Kari J. Eskola, Prof. Jouni Suhonen, Dr. Juha Merikoski, Prof. Matti Leino and Prof. Hannu Häkkinen, just to name a few.

Big thanks go to all of my studying friends and colleagues for your friendship and all the inspiring discussions we have had, physics related or otherwise. I also hope that the Holvi community will continue guarding the Baltic Sea as it has been doing for many years. Lastly, I want to thank Soila, my family and my friends for their support. This would not be possible without you.

Financial support from the Magnus Ehrnrooth Foundation, Academy of Finland, University of Jyväskylä, Nordforsk, and Ellen and Artturi Nyyssönen Foundation are gratefully acknowledged.

Author Ville Kotimäki
Department of Physics
Nanoscience Center
University of Jyväskylä
Jyväskylä
Finland

Supervisor Associate Professor Esa Räsänen
Department of Physics
Tampere University of Technology
Tampere
Finland

Reviewers Professor Edwin Kukk
Department of Physics and Astronomy
University of Turku
Turku
Finland

Senior University Lecturer Ari Harju
Department of Applied Physics
Aalto University School of Science
Espoo
Finland

Opponent Professor Viðar Guðmundsson
Science Institute
University of Iceland
Reykjavík
Iceland

Abstract

In this thesis, electron transport in two dimensions with perpendicular magnetic field is studied in three different nanodevices. The devices of interest are quantum rings, Fabry-Perót interferometers in the integer quantum Hall regime, and a stadium-shaped quantum dot. The method used in this thesis combines time-dependent dynamics, realistic modeling of the sample geometry, and the electron-electron interactions. The combination forms a more realistic numerical simulation for the magnetoconductance than what has been previously achieved. Understanding interference effects and the related phenomena might be useful in designing future computer architectures, for example.

Electron dynamics is examined by solving the time-dependent Schrödinger equation numerically in a real-space grid and, in the presence of electron-electron interactions, with the use of time-dependent density-functional theory. The simulations are carried out with the `OCTOPUS` code that allows the construction of arbitrary model potentials for experimental nanostructures.

The first study is the time-dependent discharge simulation of a quantum ring. We find clear Aharonov-Bohm oscillations with a single transport loop but also oscillations that arise from multiple transport loops. The effect of electron-electron interactions in Aharonov-Bohm oscillation is relatively weak, but the oscillation visibility strongly depends on the ring width. Our results suggest that the current flows through thin conduction channels and is dominated by only a few electrons when the Aharonov-Bohm oscillation is successfully measured.

The second study examines transport characteristics of a realistic quantum Hall-based Aharonov-Bohm interferometer. First, the electron density is solved self-consistently for the given experimental structure. The resulting electron density is used to determine the distribution of the current-carrying incompressible strips which are used as a base for the transport model. The transport simulations show clear Aharonov-Bohm oscillations whose amplitude has an optimal value when the distance between the channels and the channel width are chosen suitably. The electron-electron interactions do not suppress the visibility of the Aharonov-Bohm oscillations, but induce a channel separation dependent phase shift. Our results indicate that Aharonov-Bohm interferometers can, in principle, be used as a controllable current switches.

Finally, we examine the magnetoconductance fluctuations of a stadium-shaped, classically chaotic quantum dot. We find self-similar conductance fluctuations in more than two orders of magnitude. The detrended fluctuation analysis and variance method are used to calculate the fractal dimension of the conductance fluctuations. Our results are in good qualitative agreement with experimental results.

List of publications

This thesis is based on the work contained in the following publications:

I V. Kotimäki and E. Räsänen, *Aharonov-Bohm effect in many-electron quantum rings*, Physical Review B **81**, 2453126 (2010).

II V. Kotimäki, E. Cicek, A. Siddiki, and E. Räsänen, *Time-dependent transport in Aharonov-Bohm interferometers*, New Journal of Physics **14**, 053024 (2012).

III A. Salman, V. Kotimäki, A. Siddiki, and E. Räsänen, *Many-electron transport in Aharonov-Bohm interferometers: A time-dependent density-functional study*, European Physical Journal B **86**, 155 (2013).

IV V. Kotimäki, E. Räsänen, H. Hennig and E. J. Heller, *Fractal dynamics in chaotic quantum transport*, Physical Review E **88**, 022913 (2013).

The author has carried out the main part of the numerical work in publications I, II and IV and participated in the calculations of article III. He has written the main drafts of articles I, II and IV, and participated in the writing of publication III.

Contents

Chapter 1

Introduction

The first recorded observations of electricity date back to 2750 BC in ancient Egypt, where people were aware of shocks from the *Thunderer of the Nile*, alias the electric catfish [1]. For hundreds of years, electricity was only an intellectual curiosity and did not play any major role in society. The interest in researching electricity ignited during the 17th century leading to the major inventions of the 19th century, i.e., the telephone, the incandescent lamp, and the discovery of the dynamo and its applicability as a generator for electric power. The latter was the key part of the second industrial revolution before the First World War.

The main carrier of electric current, the electron, was observed in 1897 by J. J. Thomson and it became the first elementary particle to be discovered [2]. The conducted experiment showed that cathode rays were particles instead of waves, atoms or molecules, and the electron charge-to-mass ratio e/m was determined with good accuracy. When the properties of electrons were investigated even further, it accelerated the formulation of quantum mechanics during the first half of the 20th century.

The first quantum theories considered the quantization of energy and light. In 1901, Max Planck explained the light emitted by the black-body radiation by proposing that the energy is quantized, i.e., can only be transfered in discrete amounts [3]. In 1919, he was awarded the physics Nobel Prize of 1918 for the discovery of the energy quanta. Four years after Planck's discovery, Albert Einstein explained the photoelectric effect by postulating that all electromagnetic radiation can be viewed as particles of energy, which were later given the name *photon*. Modern quantum theory was initiated by de Broglie in 1925, when he postulated that all matter could behave like waves [4]. De Broglie's ideas were used as a starting point when Erwin Schrödinger formulated wave mechanics and the non-relativistic Schrödinger equation in 1926 [5]. In 1927, Werner Heisenberg stated that there is a relation for the theoretical maximum accuracy of the simultaneous measurement for complementary physical quantities [6]. In addition to the *uncertainty principle*, Heisenberg participated in the formulation of the linear algebra of quantum mechanics.

The wave nature of the electron was measured in 1927 by Davisson and

Germer [7], and the electron spin was observed to be half-integer in 1925 by Goudsmit and Uhlenbeck [8]. The statistical properties of electrons and their relativistic theory were determined in 1925 by Pauli [9], and Fermi [10], and in 1928 by Dirac [11]. A distinctive macroscopic phenomenon arising from quantum effects is superconductivity discovered by H. K. Onnes already in 1911. He measured the resistance of solid mercury at the temperature of 4.2 K and noticed that the resistance of the sample disappeared completely when the sample was cooled below its critical temperature [12]. The microscopic theory of this peculiar phenomenon followed much later in 1957, when Bardeen, Cooper, and Schrieffer explained the superconducting current through boson-like Cooper pairs formed by two separated electrons via the electron-phonon interaction [13]. Both the discovery and the thoery were awarded with physics Nobel Prizes in 1913 and 1972, respectively.

Nowadays, the majority of applied electronic devices are based on semiconducting materials, e.g. silicon and gallium arsenide. The reason why semiconductors are widely used in electronics industry is that their conductance can be easily varied by even several orders of magnitude. This is usually done by controlled inclusion of disorder atoms to add or remove conduction electrons, i.e., by doping, or by varying the voltage of certain control electrodes near the conduction channel, i.e., by gating. The most widely used semiconductor device is the transistor which is used to amplify and switch electric signals, and it is the main building block of computer processors and other integrated circuits. The point contact transistor was developed by John Bardeen and Walter Brattain who were studying the metal-semiconductor interface effects in 1947. They were awarded the Nobel Prize in physics in 1956 "for their researches on semiconductors and their discovery of the transistor effect", together with William Shockley who had developed a junction transistor.

The recent development of electronics industry has mostly been due to the increased ability to miniaturize the size of the components as predicted by Moore's law. The law states that the number of transistors on integrated circuits doubles in approximately every two years [14], and has predicted the evolution of integrated circuits for almost 50 years. The trend is expected to continue in the near future, but the lithography techniques used to fabricate the devices are approaching their intrinsic physical limits. Thus, the miniaturization cannot continue much further by using the current designs unless new ideas are developed.

One way to explore new electron transport phenomena is to restrict the movement of electrons. For example, by combining two layers of different semiconducting materials a thin layer of conduction electrons is formed at the interface of the materials. In this way, the movement of the electrons is effectively confined in two dimensions. The two-dimensional electron gas can also be formed on a sheet structure like graphene [15] or on the surface of a suitable material, e.g., topological insulators [16].

The most notable effect arising from the confinement of the electron movement is the quantum Hall effect measured in 1980 by Klaus von Klitzing *et al.* [17]. In the quantum Hall effect, the perpendicular voltage across the Hall bar has a step-like behavior with extremely precise values on plateaus characterized by integers as a function of the magnetic field. In addition, the longitudinal resistance vanishes whenever the magnetic-field value corresponds to the plateau. It was later found out by Laughlin, Tsui, and Störmer [18, 19] that there are more plateaus corresponding to fractional indices at higher magnetic fields. The discoveries of the integer and fractional quantum Hall effects led to two Nobel Prizes in physics given to von Klitzing in 1985 and to Laughlin, Tsui, and Störmer in 1998.

When the movement of electrons is restricted even further by adding gate electrodes to confine the two-dimensional electron gas, a structure called a quantum dot is formed. Its size is typically in the range between 10 nm and 500 nm and the dot contains a tunable number of electrons from one up to thousands. Due to the advances in the semiconductor research during 1980s, sufficiently high mobilities to produce samples with the elastic mean free path exceeding the sample size can be fabricated. In these samples electron transport is ballistic, i.e., not affected by scattering from impurities but only the sample geometry which can be varied by tuning the gate voltages. In addition, the gate voltages can be used to vary the number of electrons in the quantum dot and its coupling to the leads. If the point contacts are squeezed away by adjusting the gate voltages, the spectrum of the quantum dot becomes discrete and the dot can be viewed as an artificial atom. Quantum dots display many features seen in other systems such as small metallic nanoparticles and carbon fullerene molecules, so they can be used as a general model for coherent quantum structures. Etching, molecular-beam epitaxy, electron lithography, and self-assembly techniques are used to fabricate the quantum-dot structures [20, 21].

This thesis focuses on electron transport properties in quantum dots confined in the two-dimensional electron gas in magnetic fields. The structures of interest are quantum rings, Fabry-Pérot interferometers, and stadium-shaped quantum dots. The simulations are carried out by numerically solving the time-dependent Schrödinger equation and by the use of the time-dependent density-functional theory. The introduction part of the thesis is divided in two parts. The first part, Chapter 2, focuses on explaining the theoretical background and the physical phenomena. The second part, Chapter 3, displays the simulation results and a comparison to previous experimental and theoretical data. Finally, a summary and a short outlook are given in Chapter 4.

Chapter 2

Theory

2.1 Identical particles

In classical mechanics, we can give a unique name for each identical particle and follow their dynamics while keeping track of which particle is which. On the contrary, in quantum mechanics this labeling procedure is not possible and there is no way to distinguish identical particles from each other. This leads to different statistical distributions compared to the classical ones. It turns out that there are two different kinds of particles that can be characterized by the symmetry properties of quantum mechanical state vectors. The two particle families are called *bosons*, for which the state vector is symmetric with respect to the particle exchange,

$$|n,m\rangle = |m,n\rangle, \tag{2.1}$$

and *fermions*, for which the state vector is antisymmetric,

$$|n,m\rangle = -|m,n\rangle. \tag{2.2}$$

The antisymmetricity of the fermionic state vector gives an important result if two particles occupy the same quantum mechanical state:

$$|n,n\rangle = -|n,n\rangle \Rightarrow |n,n\rangle = 0. \tag{2.3}$$

This means that two identical particles cannot occupy the same state. The result is called the *Pauli exclusion principle.* In this thesis we examine the quantum mechanical transport properties of electrons that belong to the family of fermions.

2.2 Many-body Hamiltonian

The backbone of the nonrelativistic quantum mechanical modeling is the time-dependent Schrödinger equation (TDSE) given in atomic units (a.u., see section 2.8) as

$$\hat{H}|\Psi\rangle = i\frac{\partial}{\partial t}|\Psi\rangle, \tag{2.4}$$

where $\hat{H}$ is Hamiltonian operator, i.e., the total energy operator and $|\Psi\rangle$ is the state vector that contains all the information about the system. For an N-electron system, the Hamiltonian can be split as

$$\hat{H} = \hat{T} + \hat{V} + \hat{W}, \tag{2.5}$$

where $\hat{T}$, $\hat{V}$, and $\hat{W}$ are the kinetic energy, external potential, and interaction operators, respectively. In the position representation, these three operators can be written as

$$\begin{aligned} \hat{T} &= -\frac{1}{2}\sum_{j=1}^{N}\nabla_j^2; &(2.6)\\ \hat{V} &= \sum_{j=1}^{N} v(\mathbf{r}_j); &(2.7)\\ \hat{W} &= \frac{1}{2}\sum_{j\neq k} w(\mathbf{r}_j, \mathbf{r}_k), &(2.8) \end{aligned}$$

where $v(\mathbf{r})$ is the external potential and $w(\mathbf{r}_j, \mathbf{r}_k)$ is the interaction potential between electrons j and k. From now on, the position representation will be used unless stated otherwise.

The solution of the TDSE is generally, i.e., with more than a few particles, complex and must be obtained numerically. In two dimensions, the wave function for N particles contains $2N$ position coordinates. For example, calculations for six interacting particles in a real-space grid of 500 points per coordinate axis require roughly $500^{12} \sim 10^{32}$ grid points, which is way beyond the memory capacity of any modern computer hardware. Luckily, there are some clever ways to rewrite the many-particle problem and reduce the memory requirements.

2.3 Density-functional theory

Density-functional theory (DFT) is one of the most popular methods to reformulate the many-particle problem to a more easily calculable form. It is built on the result stating that through a one-to-one mapping between the ground-state wave functions and densities (see below), all the ground-state properties can be deduced from the density only. This reduces the required position coordinates from $D \times N$ to D (where D is the dimension) which in turn lowers the computational cost dramatically. The theorems behind this result were proved by Pierre Hohenberg and Walter Kohn in 1964 [22] and, together with several further contributions, led to the 1998 Nobel Prize in chemistry awarded to Walter Kohn together with John Pople for their development of the DFT and computational methods in quantum chemistry, respectively.

Nowadays, DFT calculations are done by the use of the Kohn-Sham construction [23] (see Sec. 2.3.2), where the system of interest is replaced by a non-interacting system in an effective potential. The effective potential adjusts the non-interacting system in such a way that the orbitals from the noninteracting system produce the same density as in the interacting system of interest. In principle, the theory is exact but in practice some approximations are required.

Conventionally, DFT has been used heavily in the field of quantum chemistry but since 1990s it has gained increasing popularity in material science and solid-state physics. The number of published DFT articles in 2011 was over 8000 and the yearly number is expected to reach 10000 in the next few years. Applications of DFT range from the prediction of new catalysts to new Li battery materials and protein folding [24].

2.3.1 Hohenberg-Kohn theorem

The proof of the Hohenberg-Kohn theorem proceeds in two parts. First, it is proven that there is a one-to-one correspondence between the external potential and the ground-state wave function. Potentials and wave functions are considered different if they differ by more than a constant $\hat{V}_1 \neq \hat{V}_2 + C, C \in \mathbb{R}$ or a constant phase factor $\Psi_1 \neq e^{i\phi}\Psi_2,\ \phi \in \mathbb{R}$, respectively. The proof proceeds by *reductio ad absurdum.* Suppose that there are two different potentials $\hat{V}_1$ and $\hat{V}_2$ that produce the same ground state $|\Psi\rangle$. We get

$$\begin{aligned} \hat{H}_1\Psi &= (\hat{T} + \hat{V}_1 + \hat{W})\Psi = E_1\Psi; \\ \hat{H}_2\Psi &= (\hat{T} + \hat{V}_2 + \hat{W})\Psi = E_2\Psi. \end{aligned}$$

If we substract both equations we get

$$(\hat{V}_1 - \hat{V}_2)\Psi = (E_1 - E_2)\Psi = C\Psi, \tag{2.9}$$

where $C \in \mathbb{R}$ is a constant. For non-zero wave functions and only position dependent potential operators, we can divide Ψ out and get $\hat{V}_1 = \hat{V}_2 + C$, which is in contradiction with our assumption. Therefore our assumption must be wrong and there is one-to-one correspondence between potentials and ground state wave functions.

The second part of the proof shows that there is a one-to-one correspondence between the ground-state densities and ground-state wave functions. The proof is constructed again with *reductio ad absurdum.* Suppose that there are at least two different quantum mechanical states with corresponding Hamiltonians that produce the same ground state density. Then we get

$$\begin{aligned} E_1 &= \langle\Psi_1|\hat{H}_1|\Psi_1\rangle = \langle\Psi_1|\hat{H}_2 + \hat{V}_1 - \hat{V}_2|\Psi_1\rangle \\ &= \langle\Psi_1|\hat{H}_2|\Psi_1\rangle + \int \mathrm{d}\mathbf{r}\; n(\mathbf{r})[v_1(\mathbf{r}) - v_2(\mathbf{r})] \\ &> E_2 + \int \mathrm{d}\mathbf{r}\; n(\mathbf{r})[v_1(\mathbf{r}) - v_2(\mathbf{r})], \end{aligned}$$

where we have used $\langle\psi|\hat{H}_2|\psi\rangle > E_2$ if $|\Psi\rangle$ is not the ground state of $\hat{H}_2$. A similar expression can be derived for E_2 by interchanging the indices:

$$E_2 > E_1 + \int \mathrm{d}\mathbf{r}\; n(\mathbf{r})[v_2(\mathbf{r}) - v_1(\mathbf{r})]. \tag{2.10}$$

If we sum these equations we get $E_1 + E_2 > E_1 + E_2$ which is false. Therefore, our initial assumption must have been wrong. Combining these two results we find the one-to-one correspondence between ground state densities and external potentials.

2.3.2 Kohn-Sham construction

Since there is a one-to-one correspondence between the external potential, ground-state wave function and the density, any expectation value calculated from the ground state must be a functional of the density. For the ground state energy we have

$$\begin{aligned} E_{v_0}[n] &= \langle\Psi[n]|\hat{H}_{v_0}|\Psi[n]\rangle \\ &= \langle\Psi[n]|\hat{T} + \hat{W}|\Psi[n]\rangle + \int \mathrm{d}\mathbf{r}\; n(\mathbf{r})v_0(\mathbf{r}) \\ &= F_{\mathrm{HK}}[n] + \int \mathrm{d}\mathbf{r}\; n(\mathbf{r})v_0(\mathbf{r}), \end{aligned}$$

where $F_{\mathrm{HK}}[n]$ is a called the Hohenberg-Kohn functional and it is the same for all systems containing the same interaction (here Coulombic, i.e., $\hat{W} = 1/|\hat{\mathbf{r}} - \hat{\mathbf{r}}'|$) between particles. An expression for $F_{\mathrm{HK}}[n]$ can be found by examining the auxilary non-interacting *Kohn-Sham* (KS) system, with the Hamiltonian

$$\hat{H}_s = \hat{T} + \hat{V}_s[n], \tag{2.11}$$

where $\hat{V}_s[n]$ is the effective potential chosen in such a way that the eigenstates of the auxiliary non-interacting Hamiltonian produce the same density as the interacting system. The ground-state wave function Φ_s of the auxiliary system is called the KS wave function and can be written as a Slater determinant

$$\Phi_s[n](\mathbf{r}_1\sigma_1, ..., \mathbf{r}_N\sigma_N) = \sum_S (-1)^S \varphi_1(\mathbf{r}_{S_1}\sigma_{S_1})...\varphi_N(\mathbf{r}_{S_N}\sigma_{S_N}), \tag{2.12}$$

where the sum goes through all permutations of N indices, $(-1)^S$ yields 1 and -1 for even and odd permutations, respectively. In this work, we consider *spin-compensated* (total spin zero) systems and the wave function attains the form

$$\Phi_s[n](\mathbf{r}_1\sigma_1, ..., \mathbf{r}_N\sigma_N) = \sum_S (-1)^S \phi_1(\mathbf{r}_{S_1})\delta_{\sigma_{S_1},\uparrow}\phi_1(\mathbf{r}_{S_2})\delta_{\sigma_{S_2},\downarrow}...\phi_{N/2}(\mathbf{r}_{S_N})\delta_{\sigma_{S_N},\downarrow}. \tag{2.13}$$

The single-particle states ϕ_i are called the KS orbitals and they can be used to obtain the total density of the system as

$$n(\mathbf{r}) = 2\sum_{i=1}^{N/2} |\phi_i(\mathbf{r})|^2. \tag{2.14}$$

The total energy of the KS system is

$$E_s[n] = \langle \Phi_s[n]|\hat{T} + \hat{V}_s[n]|\Phi_s[n]\rangle = T_s[n] + \int \mathrm{d}\mathbf{r}\ v_s(\mathbf{r})n(\mathbf{r}), \tag{2.15}$$

where the KS kinetic energy functional is

$$T_s[n] = \sum_{i=1}^{N/2} \int \mathrm{d}\mathbf{r}\ |\nabla\phi_i(\mathbf{r})|^2, \tag{2.16}$$

and it is a functional of the density because the KS orbitals depend on the total density via the effective potential. The KS kinetic energy functional can be used to define the exchange-correlation energy as

$$E_{xc}[n] = F_{\mathrm{HK}}[n] - T_s[n] - E_H[n], \tag{2.17}$$

where $E_H[n]$ is the Hartree potential energy, i.e., the classical electrostatic enery defined as

$$E_H[n] = \frac{1}{2}\int \mathrm{d}\mathbf{r}\,\mathrm{d}\mathbf{r}'\ n(\mathbf{r})n(\mathbf{r}')w(\mathbf{r},\mathbf{r}'). \tag{2.18}$$

The exchange-correlation energy contains all the nontrivial parts of the energy functional and it can be divided into two parts

$$\begin{aligned} E_{xc}[n] &= E_x[n] + E_c[n]; & (2.19)\\ E_x[n] &= \langle \Phi_s[n]|\hat{W}|\Phi_s[n]\rangle - E_H[n], & (2.20) \end{aligned}$$

where the exchange energy can be written for a spin-compensated system as a Fock integral for the KS states

$$E_x[n] = -\sum_{i,j=1}^{N/2} \int \mathrm{d}\mathbf{r}\,\mathrm{d}\mathbf{r}'\ \phi_i^*(\mathbf{r})\phi_j^*(\mathbf{r}')w(\mathbf{r},\mathbf{r}')\phi_i(\mathbf{r}')\phi_j(\mathbf{r}). \tag{2.21}$$

$E_x[n]$ is thus the energy related to the particle exchange in the KS system and the correlation energy $E_c[n]$ is all that is left after subtracting E_x from E_{xc}. The exchange energy is negative, because it takes the Pauli exclusion principle into account and prohibits electrons occupying the same orbitals, thus reducing the interaction energy from the Hartree approximation. In practice, E_{xc} needs to be approximated as discussed in the next section.

The next step in solving the many-body ground-state problem is to require that the ground-state density minimizes the total energy functional. This is done by setting the functional derivative of $E[n]$ to be zero for the all density variations which conserve the particle number,

$$\frac{\delta E_{v_0}[n]}{\delta n(\mathbf{r})} = 0. \tag{2.22}$$

This leads to a defining equation for the effective potential,

$$v_s[n](\mathbf{r}) = v_0(\mathbf{r}) + v_H[n](\mathbf{r}) + v_{xc}[n](\mathbf{r}), \tag{2.23}$$

where the Hartree and exchange-correlation potentials are defined as

$$v_H[n](\mathbf{r}) = \frac{\delta E_H[n]}{\delta n(\mathbf{r})} = \int \mathrm{d}\mathbf{r}'\ n(\mathbf{r}')w(\mathbf{r},\mathbf{r}'), \tag{2.24}$$

and

$$v_{xc}[n](\mathbf{r}) = \frac{\delta E_{xc}[n]}{\delta n(\mathbf{r})}, \tag{2.25}$$

respectively. Now that we have an expression for the effective potential $v_s[n](\mathbf{r})$, we can, in principle, obtain the ground-state density and energy by solving the *Kohn-Sham equations* self-consistently:

$$\Big[-\frac{1}{2}\nabla^2 + v_s[n](\mathbf{r})\Big]\phi_i(\mathbf{r}) = \epsilon_i\phi_i(\mathbf{r}); \tag{2.26}$$

$$n(\mathbf{r}) = 2\sum_{i=1}^{N/2} |\phi_i(\mathbf{r})|^2; \tag{2.27}$$

$$v_s[n](\mathbf{r}) = v_0(\mathbf{r}) + v_H[n](\mathbf{r}) + v_{xc}[n](\mathbf{r}). \tag{2.28}$$

Here Eq. (2.26) is the Schrödinger equation for the KS Hamiltonian (2.11). The challenge in using DFT is to find a good approximation for the exchange-correlation, which is generally unknown except for specific systems such as the homogeneous electron gas.

2.3.3 Pair density and the exchange-correlation hole

The pair density, which gives the probability per unit area squared to find particles at positions $\mathbf{r}$ and $\mathbf{r}'$, is defined as

$$\Gamma(\mathbf{r},\mathbf{r}') = \frac{1}{(N-2)!}\sum_{\sigma,\sigma',\sigma_3,\ldots,\sigma_N}\int \mathrm{d}\mathbf{r}_3 \ldots \mathrm{d}\mathbf{r}_N\ |\Psi(\mathbf{r}\sigma,\mathbf{r}'\sigma',\mathbf{r}_3\sigma_3,\ldots,\mathbf{r}_N\sigma_N)|^2. \tag{2.29}$$

With the pair density we can write the conditional probability density $\rho(\mathbf{r}|\mathbf{r}')$ to find a particle at $\mathbf{r}$ when there is another particle at $\mathbf{r}'$ as

$$\rho(\mathbf{r}|\mathbf{r}') = \frac{\Gamma(\mathbf{r},\mathbf{r}')}{n(\mathbf{r}')}. \tag{2.30}$$

If the particles are completely uncorrelated we have $\rho(\mathbf{r}|\mathbf{r}') = n(\mathbf{r})$. The exchange-correlation hole is defined as

$$\rho_{xc}(\mathbf{r}|\mathbf{r}') = \rho(\mathbf{r}|\mathbf{r}') - n(\mathbf{r}) = \frac{\Gamma(\mathbf{r},\mathbf{r}')}{n(\mathbf{r}')} - n(\mathbf{r}), \tag{2.31}$$

that satisfies the sum rule

$$\begin{aligned}\int \mathrm{d}\mathbf{r}\ \rho_{xc}(\mathbf{r}|\mathbf{r}') &= \frac{1}{n(\mathbf{r}')}\int \mathrm{d}\mathbf{r}\ \Gamma(\mathbf{r},\mathbf{r}') - \int \mathrm{d}\mathbf{r}\ n(\mathbf{r}) \\ &= \frac{1}{n(\mathbf{r}')}(N-1)n(\mathbf{r}') - N = -1. \qquad (2.32)\end{aligned}$$

For correlated electrons, the probability to find an electron near the reference electron is reduced compared to the uncorrelated electron density; thus the exchange-correlation hole integrates exactly to minus one electron. The exchange-correlation hole can be split into two parts as

$$\rho_{xc}(\mathbf{r}|\mathbf{r}') = \rho_x(\mathbf{r}|\mathbf{r}') + \rho_c(\mathbf{r}|\mathbf{r}'), \tag{2.33}$$

where $\rho_c(\mathbf{r},\mathbf{r}')$ is the correlation hole, and the exchange hole is defined as

$$\rho_x(\mathbf{r}|\mathbf{r}') = \frac{\Gamma_s(\mathbf{r},\mathbf{r}')}{n(\mathbf{r}')} - n(\mathbf{r}), \tag{2.34}$$

where $\Gamma_s(\mathbf{r},\mathbf{r}')$ is the pair density of the KS system. The exchange and correlation parts satisfy respective sum rules:

$$\int \mathrm{d}\mathbf{r}\ \rho_x(\mathbf{r}|\mathbf{r}') = -1; \tag{2.35}$$

$$\int \mathrm{d}\mathbf{r}\ \rho_c(\mathbf{r}|\mathbf{r}') = 0. \tag{2.36}$$

Many approximations of the exchange-correlation effects focus on the exchange part because it is simpler and it also yields higher contributions to the total energy in most systems. The exchange part can be calculated exactly through the Fock term [Eq. (2.21)], but this is computationally heavy and thus E_x is approximated in most of the functionals.

2.3.4 Exchange-correlation functionals

The simplest way to tackle the problem of the exchange-correlation energy and potential is to assume that they depend on local density values only and that the reference values of the homogeneous electron gas can be used. The resulting approximation is called the *local-density approximation* (LDA). It was first proposed in the original papers by Hohenberg, Kohn, and Sham [22, 23], and became the weapon of choice in DFT calculations in the 1970s and 1980s. It is still used today, because the results it provides are often surprisingly good, mostly because it satisfies the sum rule (2.32) for exchange and correlation, leading to error cancellation in the exchange and correlation part.

Usually LDA does not work well for highly localized systems and it tends to overestimate the chemical binding. A natural extension to LDA is to assume that in addition to the local density, the exchange-correlation energy also depends on the gradients of the density. The resulting approximation is made by doing a functional Taylor expansion to the exchange-correlation hole with respect to the density gradients. This is called the *gradient expansion approximation* (GEA) and it is valid for slowly varying densities [22, 23].

Unfortunately, the GEA does not satisfy the nonpositivity requirement of the exchange energy, nor the sum rule (2.35). The next step in approximating the exchange and correlation effects is to allow a more liberal choice of the expansion than the truncated Taylor polynomial, while retaining the local functional dependence on the density and density gradients. Such approximations are called *generalized gradient approximations* (GGAs) and there are different strategies in constructing them. The first wat, is to develop functionals based on the exact properties of the electron gas. This can be done by introducing real-space cutoffs to the GEA of the exchange hole

$$\rho_x(\mathbf{r}|\mathbf{r}+\mathbf{R}) \approx -\frac{1}{2}n(\mathbf{r})y\Theta(y)\Theta\big(R_c(\mathbf{r})-R\big), \tag{2.37}$$

where $y = y[n, \nabla n]$ is some functional of density and density gradients. The first Heaviside function is used to ensure the nonpositivity requirement of ρ_x, and the second one is used to force the sum rule (2.35) via the use of the cutoff radius $R_c(\mathbf{r})$ [25]. An equivalent treatment of the correlation energy is troublesome, so that is often approximated with the LDA [23] or *random phase approximation* [26]. Applications can be tackled with, e.g., the PBE functional, which is a commonly used simplified version of the GGA introduced in 1996 by Perdew *et al.* [27].

GGAs can be constructed also through models that satisfy important theoretical requirements and may have one or several fitting parameters. The fitting parameters can be obtained from, e.g., Hartree-Fock calculations [28] or from experimental data [29].

GGAs can also be combined with other functionals like the exact exchange or LDA. The resulting approximations are called *hybrids*. One of the most popular hybrids used by chemists today, B3LYP, is based on fitting parameters and was introduced in early 1990s by building on Becke's exchange functional [29–31]. B3LYP replaces a small part of the GGA exchange with the exact-exchange energy.

Possible extensions to GGAs include semilocal or nonlocal terms in addition to the density and density gradients. *Meta-GGAs* can be constructed by adding the Laplacian of the density $\nabla^2 n_\sigma$ or/and the kinetic energy density $\tau = \sum_i |\nabla\phi_i|^2/2$, with KS orbitals ϕ_i, to the exchange-correlation functional [32, 33]. In general, the KS orbitals can be explicitly used to construct so-called orbital functionals for the exchange and correlation [34]. A typical example of such a functional is the exact exchange (EXX), where the exact expression for the exchange energy (2.21) is used. The main challenge in developing orbital dependent functionals for E_{xc} is the fact that the KS potential (2.28) requires the calculation of calculating the functional derivatives of energy expressions. This can be done by using the chain rule of the functional derivatives, perturbation theory, and the response function χ_s of noninteracting electrons [34]. Within EXX this leads to the optimized-effective-potential scheme [35].

2.3.5 Local-density approximation

In LDA, the exchange-correlation energy and potential are locally approximated with the corresponding results for the homogeneous electron gas. We begin here by solving the 2D-KS system for N noninteracting electrons confined in an infinitely large area A. Because the electron density is assumed to be a constant, the effective potential $v_0[n](\mathbf{r})$ cannot have any variations and can be set to zero, so we get

$$-\frac{1}{2}\nabla^2\phi_i(\mathbf{r}) = \epsilon_i\phi_i(\mathbf{r}). \tag{2.38}$$

This has solutions of the form

$$\phi_{\mathbf{k}}(\mathbf{r}) = \frac{1}{\sqrt{A}}e^{i\mathbf{k}\cdot\mathbf{r}} \tag{2.39}$$

with periodic boundary conditions, where

$$\mathbf{k} = \frac{2\pi}{L}(n_1, n_2) \tag{2.40}$$

is the wave vector, n_i is an integer, $L^2 = A$, and the KS eigenvalues are given by $\epsilon_{\mathbf{k}} = |\mathbf{k}|^2/2$. Next, we consider a spin-compensated system where all the levels below the *Fermi energy* $\epsilon_{\mathrm{F}} = k_{\mathrm{F}}^2/2$ are occupied. In such a system, the total number of electrons is given by

$$N = \sum_\sigma \sum_{|\mathbf{k}|\le k_{\mathrm{F}}} 1 = 2\cdot\frac{L^2}{(2\pi)^2}\int\limits_{B(0;k_F)} \mathrm{d}\mathbf{k} = \frac{L^2}{2\pi^2}\pi k_{\mathrm{F}}^2 = \frac{Ak_{\mathrm{F}}^2}{2\pi}, \tag{2.41}$$

where we have replaced the sum over $\mathbf{k}$ vectors with an integral and the density of states. The previous expression leads to the electron density

$$\frac{N}{A} = n = \frac{k_\mathrm{F}^2}{2\pi}. \tag{2.42}$$

Next, we calculate the exchange energy from Eq. (2.21) as

$$\begin{aligned} E_x[n] &= -\sum_{|\mathbf{k}|\leq k_F}\sum_{|\mathbf{q}|\leq k_F}\int \mathrm{d}\mathbf{r}\,\mathrm{d}\mathbf{r}'\;\phi^*_\mathbf{k}(\mathbf{r})\phi^*_\mathbf{q}(\mathbf{r}')\phi_\mathbf{k}(\mathbf{r}')\phi_\mathbf{q}(\mathbf{r})w(\mathbf{r},\mathbf{r}') \\ &= -\int \mathrm{d}\mathbf{r}\,\mathrm{d}\mathbf{r}'\left[\sum_{|\mathbf{k}|\leq k_F}\phi^*_\mathbf{k}(\mathbf{r})\phi_\mathbf{k}(\mathbf{r}')\right]\left[\sum_{|\mathbf{q}|\leq k_F}\phi^*_\mathbf{q}(\mathbf{r})\phi_\mathbf{q}(\mathbf{r}')\right]^* w(\mathbf{r},\mathbf{r}') \\ &= -\frac{1}{4}\int \mathrm{d}\mathbf{r}\,\mathrm{d}\mathbf{r}'\;|\gamma_s(\mathbf{r},\mathbf{r}')|^2 w(\mathbf{r},\mathbf{r}'), \end{aligned} \tag{2.43}$$

where $\gamma_s(\mathbf{r},\mathbf{r}')$ is the one-particle density matrix of the KS system. If we plug in the plane-wave solutions to the one-particle density matrix we get

$$\begin{aligned} \gamma_s(\mathbf{r},\mathbf{r}') &= 2\sum_{|\mathbf{k}|\leq k_\mathrm{F}}\phi^*_\mathbf{k}(\mathbf{r})\phi_\mathbf{k}(\mathbf{r}') = 2\sum_{|\mathbf{k}|\leq k_\mathrm{F}}\frac{1}{A}e^{i\mathbf{k}\,\cdot\,(\mathbf{r}'-\mathbf{r})} \\ &= \frac{2}{A}\frac{A}{(2\pi)^2}\int_{B(0;k_F)}\mathrm{d}\mathbf{k}\;e^{i\mathbf{k}\,\cdot\,(\mathbf{r}'-\mathbf{r})} = \frac{1}{2\pi^2}\int_0^{k_\mathrm{F}}\mathrm{d}kk\int_0^{2\pi}\mathrm{d}\theta\;e^{iku\cos(\theta)} \\ &= \frac{1}{\pi}\int_0^{k_\mathrm{F}}\mathrm{d}k\;kJ_0(ku) = \frac{1}{\pi}\frac{k_\mathrm{F}J_1(k_\mathrm{F}u)}{u}, \end{aligned} \tag{2.44}$$

where $u = |r - r'|$ and J_i is the Bessel function of the first kind. With this result and the Coulomb potential $w(\mathbf{r},\mathbf{r}') = |\mathbf{r}' - \mathbf{r}|^{-1}$ we can calculate the exchange energy as

$$\begin{aligned} E_x[n] &= -\frac{1}{4}\int \mathrm{d}\mathbf{r}\,\mathrm{d}\mathbf{r}'\;|\gamma(\mathbf{r},\mathbf{r}')|^2 w(\mathbf{r},\mathbf{r}') \\ &= -\frac{1}{3}\int \mathrm{d}\mathbf{r}\int \mathrm{d}\mathbf{u}\left[\frac{k_\mathrm{F}J_1(k_\mathrm{F}u)}{\pi u}\right]^2\frac{1}{u} \\ &= -\int \mathrm{d}\mathbf{r}\;\frac{2k_\mathrm{F}^3}{3\pi^2} = \int \mathrm{d}\mathbf{r}\left(-\frac{4}{3}\sqrt{\frac{2}{\pi}}\right)n^{3/2}. \end{aligned} \tag{2.45}$$

The exchange potential is calculated by functional-derivation

$$\begin{aligned} \frac{\delta E_x}{\delta n(\mathbf{r}_0)} &= \lim_{\eta\to 0}\frac{E_x[n+\eta\delta(\mathbf{r}-\mathbf{r}_0)] - E_x[n]}{\eta} \\ &= -\frac{4}{3}\sqrt{\frac{2}{\pi}}\int \mathrm{d}\mathbf{r}\;\frac{3}{2}n^{1/2}\delta(\mathbf{r}-\mathbf{r}_0) \\ &= -2\sqrt{\frac{2}{\pi}}n^{1/2}. \end{aligned} \tag{2.46}$$

To move from the result of the homogeneous 2D electron gas (2DEG) to the LDA expression for the exchange potential, the constant density is replaced by the density at point $\mathbf{r}$, so we get

$$v_{x,\mathrm{LDA}}[n](\mathbf{r}) = -2\sqrt{\frac{2}{\pi}}n^{1/2}(\mathbf{r}), \tag{2.47}$$

and the total exchange energy in LDA attains the form:

$$E_{x,\mathrm{LDA}}[n] = -\frac{4}{3}\sqrt{\frac{2}{\pi}}\int \mathrm{d}\mathbf{r}\; n^{3/2}(\mathbf{r}). \tag{2.48}$$

To conclude, in the LDA results for the homogeneous electron gas are used for each space-point with the local electron density.

While the exchange energy is rather straightforward to calculate, the correlation energy is more complicated and requires numerical methods. In this thesis we use the parametrization of Attaccalite *et al.* [36] for the correlation energy and potential based on quantum Monte Carlo simulations of the 2DEG.

The performance of the LDA has been examined in detail in a review article by von Barth [37]. It is expected that the LDA works well mostly in situations where the electron density does not contain any steep density variations because then the assumption of the electron density being locally constant is better justified. However, surprisingly accurate results have been obtained with the LDA in comparison with more exact schemes such as exact diagonalization and quantum Monte Carlo for various quantum-dot systems [38–40]. The 2D-LDA functional for the exchange and correlation is used throughout this thesis unless otherwise stated.

2.3.6 Time-dependent density-functional theory

Time-dependent density-functional theory (TDDFT) was originally formulated by Runge and Gross in 1984 and applies the principles of DFT to time-dependent systems (see below). The applications of TDDFT include electronic excitations, ionization, optical response of solids, transport through single molecules, bond breaking, high-harmonic generation, multiphoton ionization, and quantum control [41].

Runge-Gross theorem

The basis of TDDFT is the Runge-Gross theorem [42], which states that there is a one-to-one correspondence between the time-dependent external potential $v_{\mathrm{ext}}(\mathbf{r}, t)$, apart from a purely time-dependent function $C(t)$, and the density $n(\mathbf{r}, t)$ for a given initial state Ψ_0. The idea of the proof is to show that if the external potentials differ more than a time-dependent constant, the resulting current densities are different and, thus, the time-evolution of the particle density is different. The proof proceeds as follows: First, it is assumed that the time-dependent external potentials are Taylor expandable around the initial time:

$$v(\mathbf{r},t) = \sum_{k=0}^{\infty} \frac{1}{k!} v_k(\mathbf{r})(t-t_0)^k. \tag{2.49}$$

The condition for two potentials having more difference than a time-dependent constant is equivalent to having the smallest integer $k_0 \geq 0$ such that

$$v_{k_0}(\mathbf{r}) - v'_{k_0}(\mathbf{r}) \neq \text{const.} \tag{2.50}$$

Next, the difference of the current densities emerging from different external potentials is calculated with the use of the equation of motion for time-independent operators $\hat{O}(\mathbf{r})$

$$i\frac{d}{dt}\langle \hat{O} \rangle = \langle \Psi(t)|[\hat{O}(\mathbf{r}), \hat{H}(t)]|\Psi(t)\rangle, \tag{2.51}$$

and density and current density operators given by

$$\hat{n}(\mathbf{r}) = \sum_l \delta(\mathbf{r}-\mathbf{r}_l); \tag{2.52}$$

$$\hat{\mathbf{j}}(\mathbf{r}) = \frac{1}{2i} \sum_l \big[\nabla_l \delta(\mathbf{r}-\mathbf{r}_l) + \delta(\mathbf{r}-\mathbf{r}_l)\nabla_l\big]. \tag{2.53}$$

The continuity equation reads

$$\frac{\partial}{\partial t} n(\mathbf{r},t) = -\nabla \cdot \mathbf{j}(\mathbf{r},t), \tag{2.54}$$

where $n(\mathbf{r},t)$ and $\mathbf{j}(\mathbf{r},t)$ are the density and the corresponding current density, which can be calculated as the expectation values of the density and the current density operators, respectively. When we proceed with the calculation we get

$$\begin{aligned} \frac{\partial}{\partial t}\big[\mathbf{j}(\mathbf{r},t) - \mathbf{j}'(\mathbf{r},t)\big]\Big|_{t=t_0} &= -i\langle \Psi_0|[\,\hat{\mathbf{j}}(\mathbf{r}), \hat{H}(t_0) - \hat{H}'(t_0)]|\Psi_0\rangle \\ &= -n(\mathbf{r},t_0)\nabla\big[v(\mathbf{r},t_0) - v'(\mathbf{r},t_0)\big], \end{aligned} \tag{2.55}$$

which implies that the current densities are different if the potentials differ at $t = t_0$. A similar result can be obtained for the $(k+1)$st time derivative of the current density difference with the use of Eq. (2.51):

$$\frac{\partial^{k+1}}{\partial t^{k+1}}\big[\mathbf{j}(\mathbf{r},t) - \mathbf{j}'(\mathbf{r},t)\big]\Big|_{t=t_0} = -n(\mathbf{r},t_0)\nabla\big[v_k(\mathbf{r}) - v'_k(\mathbf{r})\big]. \tag{2.56}$$

Next, we calculate the $(k+1)$st time derivative of the difference of continuity equations and get

$$\begin{aligned} \frac{\partial^{k+2}}{\partial t^{k+2}}\big[n(\mathbf{r},t) - n'(\mathbf{r},t)\big]\Big|_{t=t_0} &= -\nabla \cdot \frac{\partial^{k+1}}{\partial t^{k+1}}\big[\mathbf{j}(\mathbf{r},t) - \mathbf{j}'(\mathbf{r},t)\big]\Big|_{t=t_0} \\ &= \nabla \cdot \big[n_0(\mathbf{r})\nabla w_k(\mathbf{r})\big], \end{aligned} \tag{2.57}$$

where $n_0(\mathbf{r}) = n(\mathbf{r}, t_0)$ and $w_k(\mathbf{r}) = v_k(\mathbf{r}) - v'_k(\mathbf{r})$. The final part of the proof is to show that the last term of Eq. (2.57) vanishes only if $w_k(\mathbf{r}) = 0$ for all k. This can be shown by considering the following integral

$$\begin{aligned}\int \mathrm{d}\mathbf{r}\; n_0(\mathbf{r})\big[\nabla w_k(\mathbf{r})\big]^2 &= -\int \mathrm{d}\mathbf{r}\; w_k(\mathbf{r})\nabla\cdot\big[n_0(\mathbf{r})\nabla w_k(\mathbf{r})\big] \\ &\quad + \oint \mathrm{d}\mathbf{S}\cdot\big[(n_0(\mathbf{r})w_k(\mathbf{r})\nabla w_k(\mathbf{r})\big]. \qquad (2.58)\end{aligned}$$

The left-hand side of the integral equation vanishes only if $w_k(\mathbf{r}) = 0$ for all k because $n_0(\mathbf{r}) \geq 0$ and $(\nabla w_k(\mathbf{r}))^2 \geq 0$. The surface integral on the right-hand side vanishes for all physically realistic potentials, which are assumed to go to zero as $1/r$ or faster. The remaining integral on the right-hand side does not go to zero if $w_k(\mathbf{r}) \neq 0$, which implies $\nabla\cdot(n_0(\mathbf{r})\nabla w_k(\mathbf{r})) \neq 0$ and that the $(k+2)$nd time derivative of the density difference is not zero according to Eq. (2.57). Thus the densities will be different immediately after $t = t_0$. This means that there is a one-to-one correspondence with time-dependent potentials and densities for a given initial state Ψ_0 [43].

Generalizations

Now that we know there is a one-to-one correspondence between the time-dependent potentials and densities, we would like to be able to build a similar construction as in the time-independent DFT. In 1999, it was proven by van Leeuwen [44] that it is possible to replace the interacting system with an auxiliary non-interacting system which produces exactly the same electron density as the interacting system. This requires that the initial states for the systems are chosen in a way that yields the same density and its time derivative at the initial time. This result makes it formally possible to use the time-dependent KS system which is introduced in the next section.

The requirement of the Taylor expandability for time-dependent potentials was removed by Ruggenthaler and van Leeuwen [45] in 2011. The proof is based on restating the one-to-one correspondence between densities and potentials as a fixed point question, and requiring that the response function of the divergence of the internal forces is bounded.

Time-dependent Kohn-Sham scheme

In the most general case, the effective potential in the KS system depends on the initial states of the noninteracting and interacting systems and the time-dependent density,

$$v_s(\mathbf{r}, t) = v_s\left[n, \Psi_0, \Phi_0\right](\mathbf{r}, t). \qquad (2.59)$$

The systems of interest are often in the ground state at the initial time t_0 and then begin to evolve under the time-dependent potential that is switched on at time t_0. The time-dependent potential describing the evolution can be written as

$$v(\mathbf{r},t) = v_0(\mathbf{r}) + v_1(\mathbf{r},t)\Theta(t-t_0), \tag{2.60}$$

where $\Theta(t-t_0)$ is the Heaviside step function. In these situations, the initial state can be solved with (static) DFT – thus Ψ_0 and Φ_0 are both functionals of the ground-state density $n_0(\mathbf{r})$. This leads to the time-dependent effective potential which is only a functional of the (time-dependent) density, $v_s[n](\mathbf{r},t)$.

In practice, the calculation proceeds as follows. First, the initial state is calculated with the static DFT. Then, the TDSE for the KS system

$$\left[-\frac{1}{2}\nabla^2 + v_s[n](\mathbf{r},t)\right]\phi_j(\mathbf{r},t) = i\frac{\partial}{\partial t}\phi_j(\mathbf{r},t) \tag{2.61}$$

is solved with the initial condition $\phi_j(\mathbf{r},t_0) = \phi_j^0(\mathbf{r})$, where $\phi_j^0(\mathbf{r})$ is the jth orbital of the KS wave function of the ground-state. The density is again obtained from the orbitals as

$$n(\mathbf{r},t) = 2\sum_{j=1}^{N/2}|\phi_j(\mathbf{r},t)|^2 \tag{2.62}$$

and the effective potential is given by

$$v_s[n](\mathbf{r},t) = v(\mathbf{r},t) + \int \mathrm{d}\mathbf{r}' n(\mathbf{r}',t)w(\mathbf{r},\mathbf{r}') + v_{xc}[n](\mathbf{r},t). \tag{2.63}$$

One of the requirements for the exchange-correlation potential $v_{xc}[n](\mathbf{r},t)$ is that it needs to be a continuous function of time. In the most general case, the exchange-correlation potential $v_{xc}[n](\mathbf{r},t)$ depends on the whole history of the system, i.e., the density $n(\mathbf{r},t')$ at every time $t' \leq t$. In the adiabatic approximation, which is used in this thesis, the static DFT is used to define the exchange-correlation potential as

$$v_{xc}^A(\mathbf{r},t) = v_{xc}^0[n_0](\mathbf{r})\big|_{n_0(\mathbf{r})=n(\mathbf{r},t)}, \tag{2.64}$$

where $v_{xc}^0[n](\mathbf{r})$ is the ground-state exchange-correlation potential. Here, the only time-dependence comes from the density and the history of the system in the functional is omitted. This automatically satisfies the continuity requirement of the exchange-correlation potential. The adiabatic LDA is used in this work.

2.3.7 Current-density-functional theory

The previous formulation does not allow electromagnetic fields via the use of the vector potential $\mathbf{A}(\mathbf{r})$, since the proper description of magnetic-field effects needs to take orbital currents into account. In 1987, Vignale *et al.* reformulated DFT to include vector potentials and paramagnetic current densities, and showed that a set of equations similar to the KS equations can be used to solve the ground state system [46]. The theory is called current-density-functional theory (CDFT), and in addition to the exchange-correlation potential it introduces the exchange-correlation vector potential $\mathbf{A}_{xc}(\mathbf{r})$ as a new functional for the correct description of the paramagnetic current density.

In this thesis the CDFT is not used but, instead, the DFT Hamiltonian is coupled to the external vector potential by the momentum operator

$$\hat{p} = -i\nabla \;\; \rightarrow \;\; -i\nabla + \mathbf{A}(\mathbf{r}). \tag{2.65}$$

This approximation was tested by Helbig *et al.* and found out to be very accurate compared to the full-fledged CDFT for confined 2D systems [40]. We apply the same method also in the time-dependent case and omit the time-dependent effects of the exchange-correlation vector potential $\mathbf{A}_{xc}$.

2.4 Aharonov-Bohm effect

One of the most peculiar features in quantum mechanics is the fact that the states describing particles can obtain a certain phase. The phase itself does not have any direct physical realization but the phase differences between encountering particles can cause measurable effects. One of the most distinct physical phenomena which portrays the effects of these phase differences is the Aharonov-Bohm (AB) effect [47, 48]. In the AB effect, a charged particle acquires a phase shift

$$\phi = \frac{2\pi q}{h} \int\limits_{\gamma} \mathbf{A}(\mathbf{r}) \cdot \mathrm{d}\mathbf{r} \tag{2.66}$$

(in SI units) from the vector potential $\mathbf{A}(\mathbf{r})$ while traveling along the path γ, where q and h are the charge of the particle and Planck's constant, respectively. The effect of this phase shift can be measured by splitting an electron beam in the vicinity of the magnetic field and merging it together after a short distance. A schematic image of the electron beam splitting can be seen in Fig. 2.1. The total phase difference between paths γ_r and γ_l is

$$\begin{aligned}
\phi_r - \phi_l \;\; &= \;\; \frac{2\pi e}{h} \left[\int\limits_{\gamma_r} \mathbf{A}(\mathbf{r}) \cdot \mathrm{d}\mathbf{r} - \int\limits_{\gamma_l} \mathbf{A}(\mathbf{r}) \cdot \mathrm{d}\mathbf{r} \right] \\
&= \;\; \frac{2\pi e}{h} \oint\limits_{\gamma_r \vee \overleftarrow{\gamma}_l} \mathbf{A}(\mathbf{r}) \cdot \mathrm{d}\mathbf{r},
\end{aligned}$$

where the difference between path integrals forms an integral over a closed loop. With Stokes' theorem and $\nabla \times \mathbf{A} = \mathbf{B}$ we get

$$\frac{2\pi e}{h} \int\limits_{S} \mathbf{B} \cdot \mathrm{d}\mathbf{s} = 2\pi\Phi/\Phi_0, \tag{2.67}$$

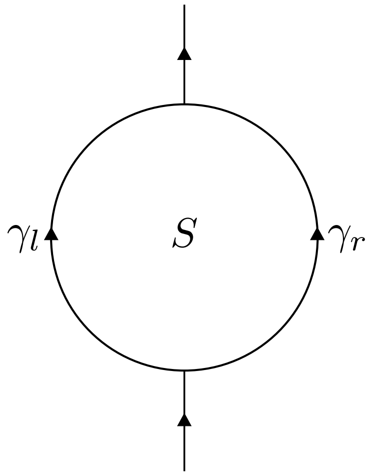

Figure 2.1: Schematic image of a formation of an Aharonov-Bohm loop with an enclosed area S in an idealized quantum ring. The electron beam moves upwards and is split in to two parts traveling through paths γ_l and γ_r. The paths are merged after a short distance and enclose the area S.

where S is the area enclosed by paths γ_r and γ_l, $\mathbf{B}$ is the magnetic field, Φ is the magnetic flux through the area S, and $\Phi_0 = h/e$ is the magnetic flux quantum. The result implies that the electrons acquire a phase difference even if they are not explicitly exposed to the magnetic field. It is enough if the magnetic field is enclosed by a current loop. The first experimental observation of the AB effect was achieved in 1960 by Chambers [49]. Electron interferometry based on the AB effect is expected to have applications in many industrial areas such as future computer technologies, physical random number generators, electron phase microscopy, and holography [50].

2.5 Quantum Hall effect

In the quantum Hall effect (QHE), the voltage V_H across the transverse direction of the 2D semiconductor device has a step-like behavior as a function of the magnetic field instead of the linear dependence obtained in the classical Hall effect (see Fig. 2.2). The step-like increase of the Hall voltage becomes visible in two-dimensional samples when the temperature is in a few-Kelvin range and the perpendicular magnetic field is sufficiently high. The longitudinal voltage V_x vanishes when V_H has a constant value and sharply peaked resistance between the steps in V_H. These oscillations in V_x are called *Shubnikov-de Haas oscillations.* The Hall voltage plateaus have a resistance $R_H = h/(e^2 M)$, where M is an integer.

The QHE was first measured in 1980 by von Klitzing *et al.* [17] who was awarded the Nobel Prize in physics in 1985. In addition to the integer quantum

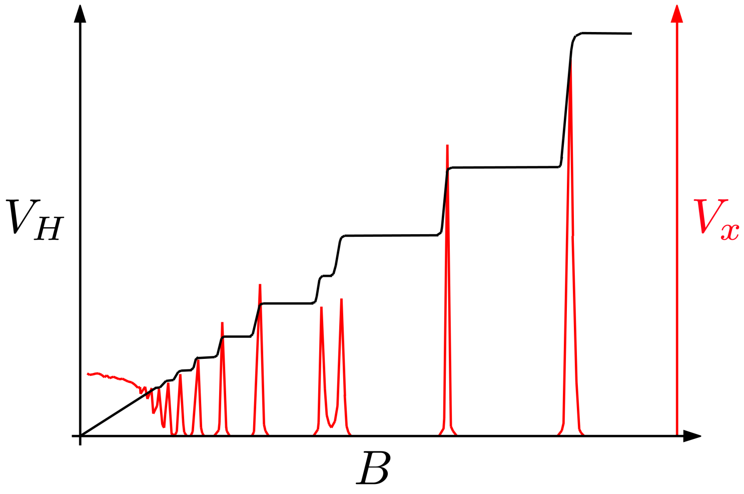

Figure 2.2: Schematic image of the voltage data in a quantum Hall measurement [51]. The Hall voltage V_H is measured in the transverse direction across the Hall bar, and the longitudinal voltage V_x is proportional to the resistance of the sample. The classical Hall effect can be seen in the lower-left part of the image where V_H increases linearly.

Hall effect (IQHE), where M is an integer, it has also been shown that M can obtain fractional values as well, leading to the fractional quantum Hall effect (FQHE). The FQHE was first measured by Tsui *et al.* [18] and explained by Laughlin [19]. The discovery and explanation of the FQHE lead to the 1998 Nobel Prize in physics being awarded to Laughlin, Tsui and Störmer. In this thesis, the transport simulations are carried out in the IQHE regime as explained in detail in the following two sections.

2.5.1 Single-electron picture

The static single-electron Schrödinger equation (SE) can be used to explain the value of the Hall resistance R_H. Let us consider the SE for conduction band electrons in the effective mass approximation (see Sec. 2.8):

$$\left\{ E_c + \frac{[\hat{\mathbf{p}} - q\mathbf{A}(\mathbf{r})]^2}{2m^*} + U(\mathbf{r}) \right\} \Psi(\mathbf{r}) = E\Psi(\mathbf{r}), \tag{2.68}$$

where E_c is the conduction band energy and $U(\mathbf{r})$ is the external confinement potential that does not include the lattice potential of the system. The external potential can be usually split in two parts as

$$U(\mathbf{r}) = U(x, y) + U_0(z), \tag{2.69}$$

which allows the separation of the single-electron SE in the z-direction as

$$\left\{E_s + \frac{[(\hat{p_x}, \hat{p_y}, 0) + \mathbf{A}(\mathbf{r})]^2}{2m^*} + U(x,y)\right\} \psi(x,y) = E\psi(x,y), \tag{2.70}$$

where $E_s = E_c + \varepsilon_m$, and ε_m is the energy contribution from the z-direction. The confinement potential is normally such that it is enough to study the first $m = 1$ state in the z-direction. Next, we assume that our system is a rectangular conductor that is uniform in the x-direction, $U(x,y) = U(y)$, and the static magnetic field points in the z-direction $\mathbf{B} = (0,0,B)$. It can be expressed in the Landau gauge through a vector potential $\mathbf{A}(\mathbf{r}) = (-By, 0, 0)$. After these substitutions Eq. (2.70) becomes

$$\left[E_s + \frac{(\hat{p}_x - By)^2}{2m^*} + \frac{\hat{p}_y^2}{2m^*} + U(y)\right] \psi(x,y) = E\psi(x,y), \tag{2.71}$$

which has a solution of the form

$$\psi(x,y) = \frac{1}{\sqrt{L}} e^{ikx} \phi(y). \tag{2.72}$$

After substituting the given solution and rearranging the terms, we get a differential equation for $\phi(y)$:

$$\left[E_s + \frac{\hat{p}_y^2}{2m^*} + \frac{1}{2} m^* \omega_c^2 (y - y_k)^2 + U(y)\right] \phi(y) = E\phi(y), \tag{2.73}$$

where $\omega_c = B/m^*$ and $y_k = k/B$. For $U(y) = 0$, Eq. (2.73) is the SE for a one-dimensional harmonic oscillator with wave functions centered at y_k and energies $E = E_s + (n + 1/2)\omega_c$. Therefore, the wave function in the xy-plane for $U(y) = 0$ is

$$\psi(x,y) = \frac{1}{\sqrt{L}} e^{ikx} u_n(q - q_k) = \langle x, y | n, k\rangle, \tag{2.74}$$

where $q = \sqrt{\omega_c}\, y$ and $q_k = \sqrt{\omega_c}\, y_k$, and

$$u_n(q - q_k) = \frac{1}{\sqrt{2^n n!}} \left(\frac{\omega_c}{\pi}\right)^{1/4} e^{-\frac{(q-q_k)^2}{2}} H_n(q - q_k), \tag{2.75}$$

where H_n is the nth Hermite polynomial.

If the magnetic field is so high that the potential $U(y)$ can be assumed to be a constant over the extent of the wave function ($1/\sqrt{\omega_c}$), the first-order perturbation theory gives

$$\begin{aligned} E(n,k) - E_s &\approx \left(n + \frac{1}{2}\right)\omega_c + \langle n, k | U(y) | n, k\rangle \\ &= \left(n + \frac{1}{2}\right)\omega_c + U(y_k). \end{aligned} \tag{2.76}$$

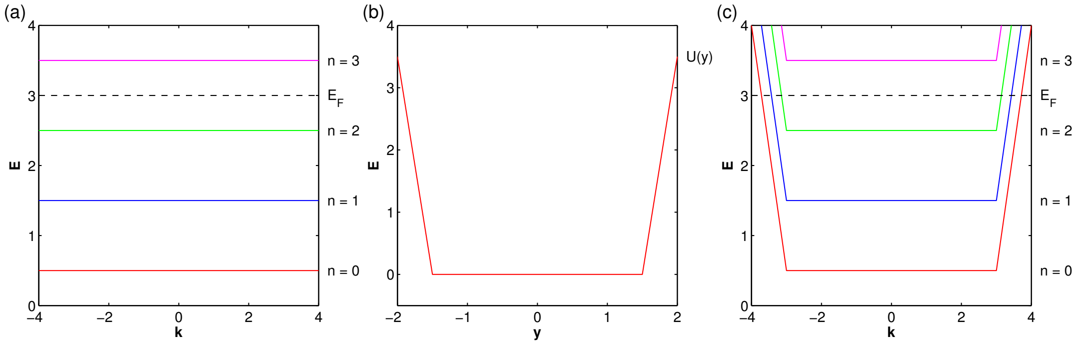

Figure 2.3: (a) Band structure, i.e., the *Landau levels* of the 2DEG in a static magnetic field. All the levels below the fermi energy E_F are occupied. (b) Schematic image of the confining potential $U(y)$ in a quantum Hall bar. (c) Band structure of confined 2DEG in a static magnetic field.

Now if we combine the Landau levels [Fig. 2.3(a)] to the external potential [Fig. 2.3(b)] we get a new dispersion relation. This relation contains states with non-zero derivatives with respect to the wave number k [see Fig. 2.3(c)], because the position of the wave function y_k is proportional to k. These states are called *edge states* and they are the current-carrying states in the quantum Hall system. This can be seen by calculating the group velocity from the dispersion relation (2.76):

$$v(n,k) = \frac{\partial E(n,k)}{\partial k} = \frac{\partial U(y_k)}{\partial k} = \frac{1}{B}\frac{\partial U(y)}{\partial y}. \tag{2.77}$$

From this expression we find that the direction of the current flow depends on the sign of the derivative of the potential for a static magnetic field, and that the forward and backward currents are flowing in opposite sides of the slab. A constant current I is imposed through the Hall bar when the Hall voltage is measured. This requires input and output leads to have different electrochemical potentials μ_L and μ_R, as depicted in Fig. 2.4, and the edge states are occupied unevenly. Measuring the increased resistance in a quantum Hall measurement requires that some of the electrons jump across the Hall bar to the other edge channel. If the semiconductor slab is sufficiently wide, and there are no unoccupied states in the middle of the sample between the energy interval $[\mu_R, \mu_L]$, the backscattering becomes prohibited and perfectly ballistic transport is observed with vanishing longitudinal resistance $R_x = V_x/I$. The number of unoccupied states within the given energy interval can be varied by tuning the strength of the magnetic field, which changes the Landau level spacing.

Next, let us calculate an expression for the ballistic current through the channel carrying electrons in equilibrium with μ_L ($> \mu_R$),

$$\begin{aligned} I &= \sum_n \int\limits_{k_R}^{k_L} \mathrm{d}k \, \frac{L_x}{2\pi} f = \sum_n \int\limits_{k_R}^{k_L} \mathrm{d}k \, \frac{1}{2\pi} \frac{\partial E(n,k)}{\partial k} \\ &= \frac{1}{2\pi} \sum_n \int\limits_{\mu_R}^{\mu_R} \mathrm{d}E = \frac{1}{2\pi} M \left(\mu_L - \mu_R\right) = \frac{M}{2\pi} V_H, \end{aligned} \tag{2.78}$$

where $v_x = L_x f$ is the group velocity of electron wave packets and M is the number of occupied edge states which quantizes the Hall voltage. From this expression we can calculate the Hall resistance $R_H = V_H/I = 2\pi/M$. In SI units we have

$$R_H = \frac{2\pi}{M} \frac{\hbar}{e^2} = \frac{h}{e^2 M}, \tag{2.79}$$

where the coefficient $R_K = h/e^2 \approx 25812.807557\ \Omega$ is called the *von Klitzing constant*. It can be measured with an extreme precision and thus it is nowadays used as the standard of resistance [52]. The spin degeneracy is omitted because the Zeeman effect separates different spin states. The Zeeman energy for spins parallel to the magnetic field in atomic units is

$$E_Z = -\frac{g_s \mu_B B}{2} = -g_s \frac{B}{4}, \tag{2.80}$$

where $g_s \approx -0.44$ is the gyromagnetic ratio of electrons in GaAs [53] and $\mu_B = 1/2$ in atomic units. The ratio of the Zeeman splitting and the Landau level spacing is

$$\frac{|2E_z|}{\omega_c} = \frac{|g_s| B/2}{B/m^*} = \frac{|g_s| m^*}{2} \approx 0.015, \tag{2.81}$$

where m^* is the effective mass in atomic units (see Sec. 2.8). Thus, the Zeeman splitting is small compared to the Landau level spacing.

2.5.2 Screening theory

Even though the single-electron edge channel picture works surprisingly well when the difference between electrochemical potentials is small compared to the Landau level spacing, there is still no commonly accepted theory of the microscopic nature of the IQHE. The experimental problems of the single-electron picture include too small relaxation rates between the edge channels and equilibration lengths that significally exceed feasible sample sizes. In addition, the single-electron picture does not take the screening and its modification in a strong magnetic field into account [54].

There are currently two different views on the subject. The bulk picture [55, 56] assumes that the electron transport occurs in the bulk and the localization effects are the reason for the quantization of current. The second view is the

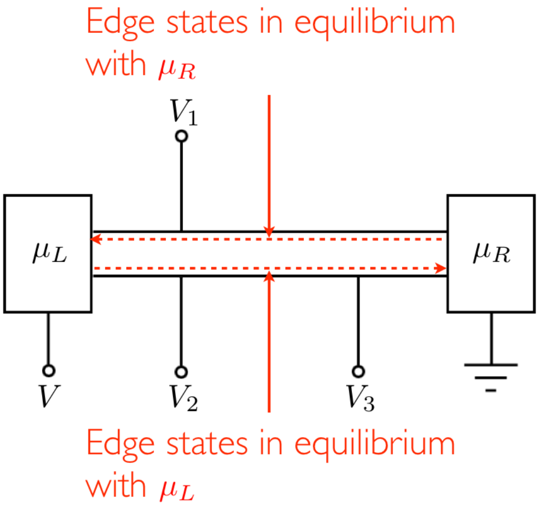

Figure 2.4: Schematic image of a quantum Hall bar. The Hall voltage and the longitudinal voltage are defined as $V_H = V_1 - V_2$ and $V_x = V_2 - V_3$, respectively.

edge channel picture [54, 57], where the effect of disorder is neglected and one-dimensional ballistic transport is assumed to occur at the sample edges leading to the quantization of current.

Filling factor

One of the key quantities in characterizing the QHE is called the filling factor and it is defined as the number of occupied Landau levels per unit area. For that we need the number of states in one Landau level, which can be calculated by considering the Landau level spacing in SI units $\hbar\omega_c$, i.e., the energy interval that is used by one Landau level. The number of states in one Landau level per unit area is

$$\hbar\omega_c D(E) = \frac{\hbar eB}{m^*}\frac{m^*}{2\pi\hbar^2} = \frac{eB}{h}, \tag{2.82}$$

where $D(E)$ is the density of states without the spin degeneracy in the 2DEG. The quantity eB/h can also be viewed as the areal density of magnetic flux quanta $\Phi_0 = h/e$. The filling factor is now defined as

$$\nu = \frac{n}{eB/h} = \frac{hn}{eB}, \tag{2.83}$$

where n is the electron density. The regions where the Fermi energy resides between Landau levels and the local filling factor is an integer are called incompressible. In incompressible regions the Landau levels are fully filled, thus restricting the rearrangement of electron distribution and keeping the electron density constant. If the Landau level is pinned to the Fermi energy, the region is called compressible and the corresponding Landau level is partially occupied.

It is commonly believed that in the edge-channel transport the current flows ballistically within the incompressible strips, which form on the edges of the semiconductor slab due to the quantizing magnetic field and direct Coulomb interactions under the correct boundary conditions. This view is supported by simulations [58, 59] and experimental evidence [60, 61].

Self-consistent Thomas-Fermi-Poisson method

The self-consistent Thomas-Fermi-Poisson approach by Güven *et al.* [58] was used to calculate the incompressible strip distribution used in this work. In this method, it is assumed that the total potential function consists of two parts,

$$V_{\mathrm{tot}}(\mathbf{r}) = V_{\mathrm{conf}}(\mathbf{r}) + V_H(\mathbf{r}), \tag{2.84}$$

where $V_{\mathrm{conf}}(\mathbf{r})$ and $V_H(\mathbf{r})$ are the confinement and the Hartree potentials, respectively. The Hartree potential is obtained by solving the Poisson equation

$$\nabla^2 V_H(\mathbf{r}) = -\frac{n_{\mathrm{el}}(\mathbf{r})}{\varepsilon_r}, \tag{2.85}$$

for a given electron distribution $n(\mathbf{r})$, permittivity ε_r, and boundary conditions. When the total potential is obtained, a new charge distribution can be calculated from the expression

$$n_{\mathrm{el}}(\mathbf{r}) = \int \mathrm{d}E \; D(E) f(E + V(\mathbf{r}) - \mu), \tag{2.86}$$

where $D(E)$ is the broadened Landau density of states, $f(x) = (1+\exp(x/k_b T))^{-1}$ is the Fermi function, and μ is the electrochemical potential.

The self-consistent calculation proceeds by iterating equations (2.85-2.86). An initial density profile is substituted into the Poisson equation (2.85), which is then used to solve the Hartree potential V_H. In turn, this is substituted into Eq. (2.86) with (2.84) to get the new electron density. The scheme is repeated until convergence is reached. The value of the electrochemical potential μ is chosen such that it produces the desired average electron density $\langle n_{\mathrm{el}} \rangle$.

2.6 Quantum chaos

The word *chaos* is understood as disorder and randomness, but in physics, chaos is something that appears to be random but is deterministic in nature. A good example of such a phenomenon affecting our lives is weather: It is fully deterministic but exceedingly nonlinear and highly dependent on the initial conditions which cannot be precisely determined. For this reason, long-term weather forecasts will remain impossible (regardless of the measuring grid and computing power). The atmospheric study *Deterministic Nonperiodic Flow* by Edward Lorenz [62] is commonly considered to be the start of the modern chaos theory.

Nonlinear systems where chaos theory is applied can be found in almost every field of science, e.g., geology, biology, computer science, economics, physics, politics, and medicine. More specific applications include, e.g., encoding private communications [63], controlling cardiac arrhythmia [64], and epileptic brain seizures [65].

Even though there is no universally accepted definition of chaos, there is one that most would agree with by Strogatz [66]:

> ”Chaos is aperiodic long-term behavior in a deterministic system that exhibits sensitive dependence on initial conditions.”

Here, *aperiodic long-term behavior* means that phase space trajectories of the system do not settle down to fixed points, periodic orbits, or quasi-periodic orbits as $t \to \infty$. Being *deterministic* means that the system's irregular behavior arises from its nonlinearity instead of noisy driving forces. In chaotic systems, nearby trajectories separate exponentially fast so that they are *sensitive to initial conditions*. This sensitivity is characterized by a positive Liapunov exponent λ defined as

$$||\delta(t)|| \sim ||\delta_0||e^{\lambda t}, \tag{2.87}$$

where δ_0 and $\delta(t)$ are the distances of the two trajectories in the phase space initially and after time t, respectively.

In quantum mechanics, all the information of the system is included in the time-dependent state vector $|\psi(t)\rangle$ that can be considered as the *trajectory* in the phase space. The squared distance between two states $|\Psi(t)\rangle$ and $|\Phi(t)\rangle$ is

$$|||\Psi(t)\rangle - |\Phi(t)\rangle||^2 = \langle\Psi(t)|\Psi(t)\rangle - 2\mathrm{Re}(\langle\Psi(t)|\Phi(t)\rangle) + \langle\Phi(t)|\Phi(t)\rangle, \tag{2.88}$$

where all inner products turn out to be constants of motion because of the linearity of the Schrödinger equation

$$\langle\psi(t_0)|\phi(t_0)\rangle = \langle\psi(t_0)|\hat{U}^\dagger(t,t_0)\hat{U}(t,t_0)|\phi(t_0)\rangle = \langle\psi(t)|\phi(t)\rangle. \tag{2.89}$$

Thus, chaos as it is defined in classical mechanics does not exist in quantum mechanics. Today the term *quantum chaos* essentially means the quantum mechanical behavior of classically chaotic systems. One of the most interesting aspects of chaos is the correspondence principle which states that the properties of a given quantum mechanical system should converge to the results from classical theory when the de Broglie wavelength is much smaller than the length scale of the system. So in principle, there should be something that could be used to distinguish chaotic systems quantum mechanically as well.

One of the methods that is used to distinguish different systems is to examine the distribution of eigenenergy level spacings. The number of energy levels $\mathrm{d}N$ with neighbouring levels within interval $[s, s+\mathrm{d}s]$ is

$$\mathrm{d}N = P(s)\mathrm{d}s, \tag{2.90}$$

where $P(s)$ is the distribution function. According to the Bohigas-Giannoni-Schmit conjecture [67], systems can be divided into three groups:

1. Systems that are classically integrable (not chaotic) follow the Poisson distribution function,
$$P(s) = A\,\exp(-\lambda s). \tag{2.91}$$
2. Systems that are classically chaotic and have time-reversal symmetry follow the eigenvalue distribution of a Gaussian orthogonal ensemble of random matrices (GOE) [68], which is approximately
$$P(s) \approx As\,\exp(-\lambda s^2). \tag{2.92}$$
3. Systems that are classically chaotic and do not have time-reversal symmetry follow the eigenvalue distribution of a Gaussian unitary ensemble of random matrices (GUE) [68], which is approximately
$$P(s) \approx As^2\,\exp(-\lambda s^2). \tag{2.93}$$

Other methods to study energy level statistics include, e.g., spectral rigidity, number variance [69], as well as detrended fluctuation analysis [70] applied in different context below.

In this work, instead of energy level statistics, we focus on transport phenomena and fractal characteristics found in chaotic systems. These issues are explained in the following section.

2.7 Fractal analysis

Many fields of modern science deal with phenomena which can be analyzed by examining the self-similarity and the nature of fluctuations and correlations within. A few examples of such phenomena are fluctuations in stock prices, shapes of different surfaces and coastlines, magnetoconductance oscillations [71], heartbeat analysis [72, 73] and even human-produced music [74–77] and gait [73, 78]. Qualifying the scaling properties of the fluctuations can help in the understanding and predict the dynamics of the system of interest. For example some heart diseases can be predicted by measuring patient's heart beat intervals [72, 73].

2.7.1 Exact self-similarity

The most typical examples of self-similarity are fractal curves that look the same in various length scales. Ideally, they are constructed from one generator block which is copied, rotated and/or mirrored, and scaled down/up infinitely many times to form the finished curve. In real world these scaling properties naturally do not hold for infinitely many scales.

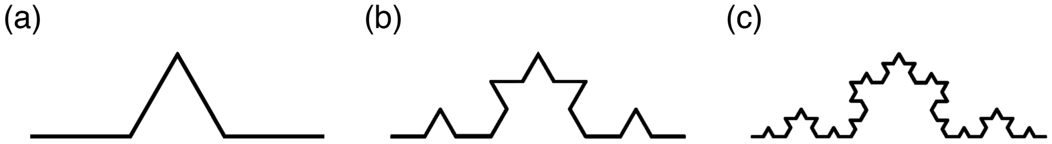

Figure 2.5: Typical example of a fractal curve is the Koch curve. The generator block (a) is scaled down with a factor of three and copied four times to generate the next level of the curve (b). The Koch curve is formed when this process is carried out repeatedly (c), in principle infinitely many times

A common way to characterize the fractality of a given curve is to calculate its fractal dimension that measures the space-filling capacity of the curve. If the curve generator can be easily obtained, the fractal dimension D is defined by

$$N = \varepsilon^{-D}, \tag{2.94}$$

where N is the number of down-scaled generators used for the next step of construction and ε is the scaling factor. In the case of the Koch curve (Fig. 2.5), $N = 4$ and $\varepsilon = 1/3$ leading to the fractal dimension $D = \log 4/\log 3 \approx 1.262$. The fractal dimension that exceeds the topological dimension of a given curve means that the curve fills the two-dimensional space more densely than an ordinary curve with equal topological and fractal dimensions.

Usually, the generator is not known or it does not even exist. This is the case, in e.g., time series analyzed below. In these situations, the previous, simple scheme to obtain the fractal dimension needs to be replaced with a more general method. The method used in this thesis, the *variation method* [79], is based on finding a suitable cover built from small sets for the graph of the function $f(x)$, and examining how the area of the cover changes when the size of the small sets is changed. Equation (2.94) needs to be modified slightly so it can be used with the covers. The area of the cover is proportional to the number of small pieces needed to construct the fractal multiplied with the area of one small two-dimensional piece of width ϵ, i.e., $A(\epsilon) \propto N\epsilon^2$. When this is plugged into Eq. (2.94) we obtain the general definition for the fractal dimension [79] as

$$D = \inf\{\eta : \epsilon^{\eta-2}A(\epsilon) \xrightarrow[\epsilon\to 0]{} 0\}. \tag{2.95}$$

In practice, the fractal dimension D is solved by assuming that $\epsilon^{\eta-2}A(\epsilon)$ is constant when $\eta = D$. With this assumption, the fractal dimension can be obtained from the slope of the linear-fit calculation of $\ln[A(\epsilon)/\epsilon^2]$ as a function of $\ln(1/\epsilon)$. In the variation method, the area of the cover $A(\epsilon)$ is called the ϵ variation (see Fig. 2.6) and its area is defined by

$$V(\epsilon, f) = \int_{x_0}^{x_1} \mathrm{d}x \; v(x, \epsilon), \tag{2.96}$$

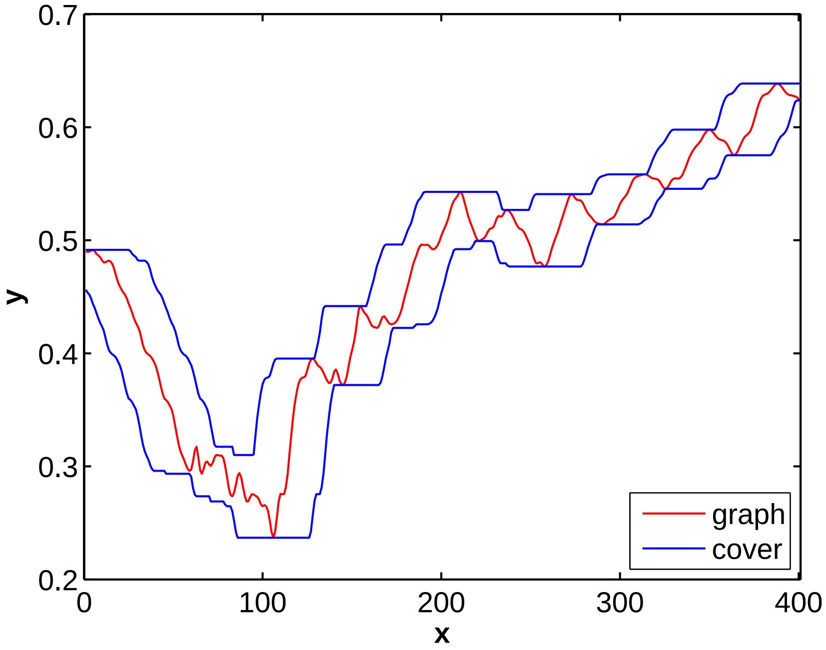

Figure 2.6: Example of a cover with $\epsilon = 20$ constructed by using the variation method with a point-wise interval shifting

where $[x_0, x_1]$ is the domain of the function $f(x)$, and $v(x, \epsilon)$ is the ϵ oscillation of the function $f(x)$ defined by

$$v(x, \epsilon) = \sup_{x' \in R_\epsilon(x)} f(x') - \inf_{x' \in R_\epsilon(x)} f(x'), \tag{2.97}$$

where $R_\epsilon(x) = \{s : |x - s| < \epsilon \text{ and } s \in [x_0, x_1]\}$. A mathematically more rigorous proof and benchmarks of the variation method can be found in Ref. [79] and references therein.

Note that when integrating the ϵ variation it is assumed that the intervals $R_\epsilon(x)$ overlap, i.e., they are shifted point-wise. Intervals can also be shifted interval-wise which produces slightly coarser cover but yields roughly the same fractal dimension. The coarser method, the *modified box-counting*, is used in the analysis of some experimental results [71].

2.7.2 Statistical self-similarity

In addition to the exact self-similarity discussed in previous section, many objects in real world are statistically self-similar. This means that their statistical properties obey similar scaling relations as the exact self-similar curves.

The definition of the statistical self-similarity in data $y(i)$ is

$$y(I_s) \overset{d}{\equiv} b^\alpha y(I_{s/b}), \tag{2.98}$$

where I_s is a set of s indices i, b is a scaling factor, and α is a scaling exponent, i.e., a self-similarity parameter. The notation $\overset{d}{\equiv}$ means that the probability distribution of the self-similar process $y(I_s)$ with scaling exponent α is the same as the properly rescaled process $b^{\alpha}y(I_{s/b})$. The proper rescaling is done by selecting s/b data points and multiplying them with a vertical scaling factor b^{α}.

This strict criterion requires the two processes of interest to have identical distribution functions, e.g., the same mean, variance, and higher moments as well. In practice, this is usually replaced by a weaker criterion and only the variances are examined.

Detrended fluctuation analysis

In this thesis, the method used to analyze statistical self-similarity in magnetoconductance curves is *detrended fluctuation analysis* (DFA) which was first used to study the organization of DNA nucleotides by Peng *et al.* [80]. Nowadays DFA is the standard method to study the so-called $1/f$ noise and long-range correlations. DFA has proven to be very reliable particularly in dealing with non-stationary time-series and trends in the data such as the heartbeat analysis [72, 73]. It deals efficiently with two typical problems observed in real world data explained in the next few paragraphs.

For an ideal self-similar process the fluctuations grow exponentially when the number of data points is increased and the process is unbounded. For real world data, this is not necessarily the case since some of the interesting processes, like the heart rate and gait, have natural upper limits. This means that after some threshold number of data points, the vertical axis does not need rescaling and the resulting self-similarity parameter α is zero.

On the other hand, the sequential order of bound data can be randomized to generate completely uncorrelated control series. For this randomized data, the resulting value for α is zero, even though the data is obviously different compared to the original bound data. This problem can be bypassed by examining the self-similarity properties of the accumulated (integrated) series instead of the original data. The integration removes the upper bound from the original series and makes it possible to differentiate it from the randomized data.

The most typical one-dimensional example of the integration is random walk. The individual steps are bound but the trajectory as an integrated series (the sum of the steps) is not and exhibits fractal scaling that can be quantified by the self-similarity parameter.

The other problem in examining the self-similarity in the fluctuations is the presence of a trend which can mask or emphasize parts of the fluctuations incorrectly. The trend can be even more pronounced when the data is integrated. For example, such a trend can be found in heart beat interval data if the physical activity varies over the measurement period. If the interest of the study is only the correlation of the heart beat timings regardless of the physical activity, the local trends need to be removed.

The standard procedure of DFA consists of the following four steps: (1) Integrating the deviation of the time series from the mean $(y(j) - \langle y \rangle)$ as

$$f(n) = \sum_{j=1}^{n} [y(j) - \langle y \rangle]\,; \tag{2.99}$$

(2) dividing integrated series into windows I_s of size s; (3) fitting with a polynomial $f_s^m(i)$ of a degree $m = 1...4$ that represents the trend in the window; and (4) calculating the standard deviation with respect to the local trend $f_s^m(i)$ from

$$\begin{aligned} \sigma(I_s) &= \sqrt{\langle (f(i) - f_s^m(i))^2 \rangle_{I_s}} \\ &= \sqrt{\frac{1}{s} \sum_{i \in I_s} [f(i) - f_s^m(i)]^2} \propto s^{\alpha}, \end{aligned} \tag{2.100}$$

where I_s is a set of indices i in windows of size s. This result $\sigma(s)$ is then obtained by averaging $\sigma(I_s)$ over all sets I_s.

The obtained value of α classifies the nature of correlations in the self-similar data [72] in the following way.

- Noise with alternating high and low values: $0 < \alpha < 0.5$
- Uncorrelated data: $\alpha = 0.5$
- Long-range correlations: $0.5 < \alpha < 1$
- $1/f$ noise: $\alpha = 1$
- Random-walk-type correlations: $\alpha = 1.5$

Algorithms for fractal analysis contain internal errors analyzed in detail by Pilgram and Kaplan [81]. DFA results for the fractal exponent are expected to have a standard deviation of $\sim 15\%$ for data sets that are of the same size as ours in this thesis.

2.8 Effective atomic units

Conventional atomic units form a system of natural units used to simplify expressions and formulae in atomic and molecular calculations. The lengths and energies are expressed with the Bohr radius $a_0 = 4\pi\varepsilon_0\hbar/(m_e e^2) \approx 0.053\,\mathrm{nm}$ and the Hartree energy $E_H = m_e e^4/(4\pi\varepsilon_0\hbar)^2 \approx 27.2\,\mathrm{eV}$. The magnetic field unit $B_H = \hbar/(e a_0^2) \approx 2.35 \cdot 10^5\,\mathrm{T}$ is obtained by setting the magnetic energy $\mu_B B_H = E_H/2$, where $\mu_B = e\hbar/(2m_e)$ is the Bohr magneton. Equations are translated to conventional atomic units by setting $m_e = 1$, $e = 1$, $\hbar = 1$ and $1/(4\pi\varepsilon_0) = 1$.

All the models considered in this thesis are constructed for two-dimensional nanodevices in AlGaAs/GaAs structures. We follow the standard scheme in modeling conduction electrons in the semiconductor heterostructure and apply the effective-mass approximation [82] with GaAs parameters, i.e., the effective mass $m^* = 0.067 m_e$ and the dielectric constant $\varepsilon_r = 12.7\varepsilon_0$. Hence, the energies, lengths, times, and magnetic fields scale as

$$\begin{aligned} E_H^* &= \frac{0.067}{12.7^2} E_H \approx 11\,\mathrm{meV} \\ a_0^* &= \frac{12.7}{0.067} a_0 \approx 10\,\mathrm{nm} \\ t_0^* &= \frac{\hbar}{E_H^*} \approx 60\,\mathrm{fs} \\ B_H^* &= \left(\frac{0.067}{12.7}\right)^2 B_H \approx 6.55\,\mathrm{T}. \end{aligned}$$

We use these *effective atomic units* in the results unless stated otherwise.

2.9 OCTOPUS code

The majority of the calculations presented in this thesis are done with the `OCTOPUS` [83–85] code package published under General Public License. The code has been built on the real-space grid discretization method which allows realistic modeling of two-dimensional nanostructures. The discretized static Schrödinger equation is solved with the conjugated-gradient algorithm.

The time-propagation is carried out by making the enforced time-reversal symmetry (ETRS) approximation for the time-evolution operator $\hat{U}(t, t_0)$. The ETRS approximation can be made after the time-evolution operator is discretized while assuming the time-dependent Hamiltonian to be constant within the time interval of interest, i.e.,

$$\hat{U}(t, t_0) \approx \exp\bigl[-i(t - t_0)\hat{H}(t)\bigr]. \tag{2.101}$$

The starting point in ETRS is the property that the forward-propagation within the time interval $\delta t/2$ of state $\psi_j(t)$ results in the same state as the backward-propagation within the same interval of the state $\psi_j(t + \delta t)$:

$$\begin{aligned} \exp\Bigl[i\frac{\Delta t}{2}\hat{H}(t + \Delta t)\Bigr]\psi_j(t + \delta t) &= \exp\Bigl[-i\frac{\Delta t}{2}\hat{H}(t)\Bigr]\psi_j(t) \\ \Rightarrow U_{\mathrm{ETRS}}(t + \Delta t, t) &= \exp\Bigl[-i\frac{\Delta t}{2}\hat{H}(t + \Delta t)\Bigr]\exp\Bigl[-i\frac{\Delta t}{2}\hat{H}(t)\Bigr], \end{aligned} \tag{2.102}$$

where $\hat{H}(t + \Delta t)$ is built from the density which is calculated from

$$\psi_j'(t + \Delta t) = \exp\Bigl[-i\Delta t\hat{H}(t)\Bigr]\psi_j(t). \tag{2.103}$$

The exponentials of the operators are expressed in Taylor series

$$\exp(\hat{A}) = \sum_{n=0}^{\infty} \frac{1}{n!} \hat{A}^n, \tag{2.104}$$

which is calculated to the fourth order in this thesis [86].

2.10 Transport scheme

The transport calculations presented in this thesis are numerical real-space simulations for the transmission factor, i.e., the probability for the electrons to travel across the device. The calculations start by calculating the initial state with the ground-state DFT. This is done with `OCTOPUS` by cutting a small portion of the input lead of the model potential. This state is then propagated through the external potential representing the device of interest. The initial velocity for the initial state is given by adding an accelerating part (linear ramp) to the external potential.

The transmission factor T, i.e., the relative number of transferred electrons, is obtained by integrating the electron density in the desired part of the calculation grid $\mathcal{A}$ for different time steps

$$T(\{a_i\}, t) = \frac{1}{N} \int\limits_{\mathcal{A}} \mathrm{d}\mathbf{r}\; n(\{a_i\}, \mathbf{r}, t), \tag{2.105}$$

where N is the number of electrons in the system and $\{a_i\}$ is a set of external parameters. The transmission factor is assumed to be proportional to the transmission coefficient available in the conventional transport theory. We repeat the calculation for all desired values for the external parameters $\{a_i\}$ to get, e.g., the magnetoconductance that can be compared with experimental data. We point out that the present scheme does not resemble the standard equilibrium transport approach in, e.g., the Landauer-Büttiker fashion [87], but it works as a qualitative tool to assess the *relative* conductance as a function of an external parameter, i.e., the magnetic field.

The calculation box is set sufficiently large so that the transmission factor has time to develop without interference caused by the reflections from the box boundaries. The density is monitored to make sure that the backscattering effects from the box boundaries do not become visible.

Chapter 3

Results

3.1 Transport in quantum rings

3.1.1 Background

Ring-shaped quantum dots, i.e., quantum rings (QRs) represent excellent examples to study the realization of the Aharonov-Bohm (AB) affect (see Fig. 3.1). The first experimental results in QR systems were obtained in submicron-diameter Au rings by Webb *et al.* in 1985 [88]. This was followed by AB measurements in semiconducting GaAs QRs in 1987 by Timp *et al.* [89]. Theoretical studies of QRs have been carried out analytically and numerically. The analytic models for QRs tend to focus on one-dimensional systems, when the width and the height of the wire-like conduction channels are zero [90–92]. This leads to electron paths which cannot be directly affected by the magnetic field in contrast with experiments [88, 89, 93, 94]. Numerical simulations include 2D tight-binding calculations [95, 96] and single-electron wave packet simulations in 2D [97–99] which, in addition to AB phase shift, are able to take the Lorentz force into account. The aim of our study [100] is to combine real-time dynamics and electron-electron interactions with the use of the time-dependent density-functional theory. The calculations are done in a 2D real-space grid which allows us to examine the role of the finite ring width (2D character) as well.

3.1.2 Model

We build a model for a single-terminal QR represented by the external potential $v_{\mathrm{ext}}(\mathbf{r})$ (see Fig. 3.2). The potential consists of the QR confinement and the output terminal which both have a Gaussian cross section $v_{\mathrm{ext,cross}}(x) \sim \exp(-x^2/a^2)$, where a determines the width of the channel. In addition, we have a linear potential across the whole device representing the source-drain voltage, and a rectangular potential well in the other end of the output terminal acting as a sink (or drain) for the electrons. The initial state for the simulation is calculated for a quantum well located in the back part of the QR (see the

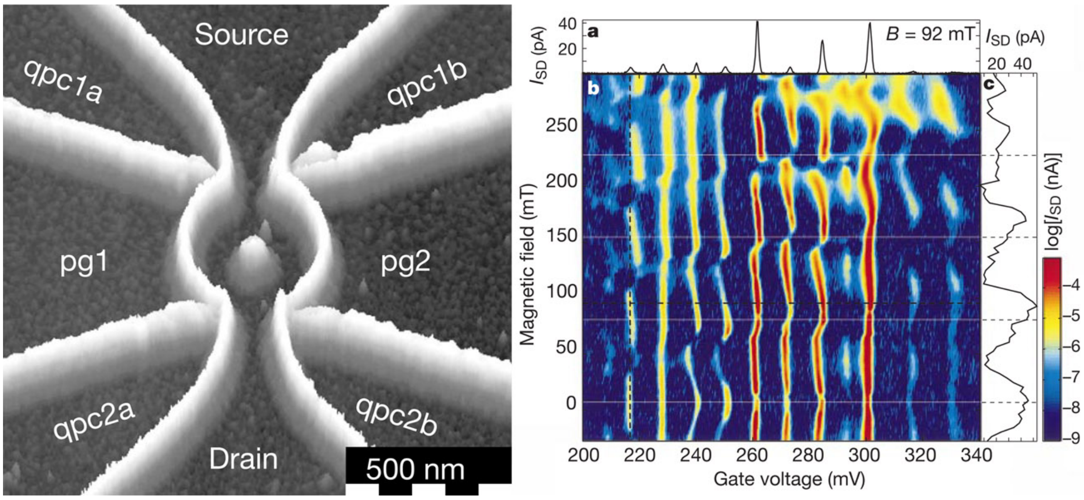

Figure 3.1: Left panel: Atomic force microscope image of QR device. Right panel: Current measurement data of the QR device with a constant source-drain voltage. (a) Gate voltage scan at a constant magnetic field. (b) Addition spectrum. (c) Magnetic field scan at a constant gate voltage shows clear AB oscillations. Experimental device and measurement data by Fuhrer *et al.* Reprinted by permission from Macmillan Publishers Ltd: Nature [93], copyright 2001.

inset of Fig. 3.2). A single-terminal device is used to minimize the undesired effects of electron backscattering at the input lead.

We calculate the transmission factor N_r as a function of time t and the magnetic flux Φ through the QR,

$$N_r(\Phi, t) = 1 - \frac{N(\Phi, t)}{N}, \tag{3.1}$$

where N is the total number of electrons in the system and $N(\Phi, t)$ is the number of electrons *inside* the QR at time t. In this study, $N_r(\Phi, t)$ is used to assess the conductivity of the device (see Sec. 2.10).

3.1.3 Transport results

We start by propagating single-electron wave packets through the QR. As an example of the dynamics, the electron density at different times with magnetic flux $\Phi = 3\Phi_0$ is visualized in Fig. 3.2. The single-electron conductivity of the device for three different channel widths at times $t = 1$ and $t = 2$ is plotted in Figs. 3.3(a) and (b), respectively. Smooth and regular AB oscillations with period Φ_0 are found at time $t = 1$. The conduction minima and maxima are positioned at magnetic flux values corresponding to phase shifts π and 2π, respectively.

The AB oscillation amplitude is considerably reduced and a phase shift of π appears when the conduction channel has its widest value $a = 1.0$. The strong

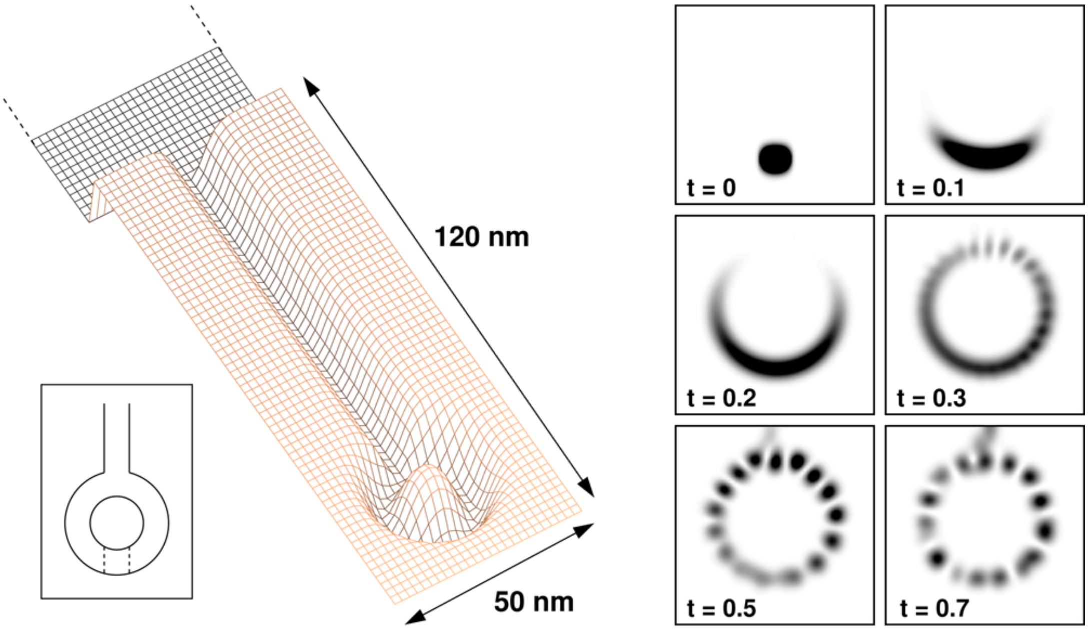

Figure 3.2: Left: External potential describing the QR. The rectangular potential well used as a sink for electrons is longer than the output lead and is not fully visible. Inset: Schematic image of the QR potential, where the potential for the initial state is outlined by the dotted line. Right: Electron density in a QR at different times with magnetic flux $\Phi = 3\Phi_0$ through the QR. The electron density distribution is not symmetrical due to the Lorentz force.

reduction in the AB oscillation amplitude as a function of the channel width is due to the suppression of the interference effects at the output lead. This occurs as a result of reduced overlap between the wave functions coming from different arms of the QR. Increasing the channel width even further eventually leads to the vanishment of AB oscillations. A similar effect due to the increasing QR width has been reported by Pichugin *et al.* [95]. The phase shift occurs due to larger transverse density variations along the conduction channels and the increased backscattering effects from the channel boundaries.

When the wave packet is propagated further in time to $t = 2$, the regular AB oscillation with the period Φ_0 is distorted by oscillations with larger frequencies. The presence of the oscillations can be verified by Fourier transforming the data in Figs. 3.3(a) and (b) which is presented in Figs. 3.3(c) and (d), respectively. At $t = 1$, the Fourier spectrum clearly shows that the oscillations contain only the component with the period Φ_0 for all channel widths. At $t = 2$, components corresponding to periods $\Phi_0/2$ and $\Phi_0/3$ appear. The oscillations with period Φ_0/n, where n is an integer, appear when parts of the electron wave packet circle the ring structure multiple times before interfering at the output lead. Similar results have been obtained in recent tight-binding [96] and wave packet [98] calculations as well as in an experimental study by Chang *et al.* [94]. The

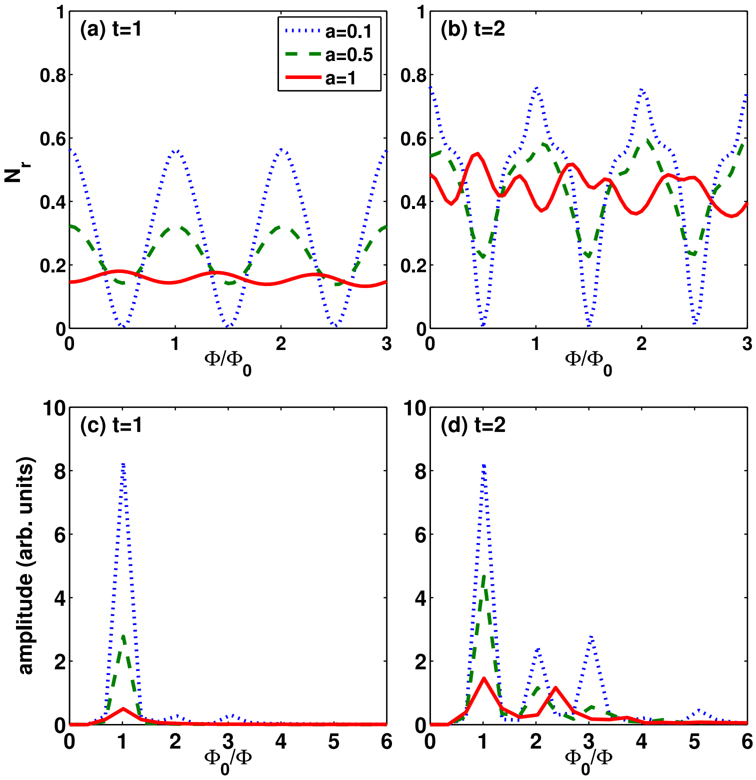

Figure 3.3: Single-electron conductivity of the QR as a function of the normalized magnetic flux Φ/Φ_0 at times (a) $t = 1$ and (b) $t = 2$. The Fourier transform of situations in (a) and (b) are depicted in (c) and (d), respectively. Larger values of a correspond to wider channels.

effect of the Lorentz force can be seen as an asymmetric density distribution along the quantum ring arms in Fig. 3.2. The other arm is slightly favored by the perpendicular magnetic field but the effect is not visible in the conductance. In a two-terminal device the conductance would be affected by the Lorentz force as the magnetic field enhances the transmission in the input lead contact by deflecting the electron density in one of the quantum ring arms, and thus suppressing the backscattering to the input lead [97].

Next we examine many-electron transport with and without electron-electron interactions, where in the interacting case, the exchange and correlation effects are handled with the local-density approximation (LDA). AB oscillations are still present but the system becomes more sensitive to the width of the channels, i.e., increasing the channel width reduces the AB oscillation amplitude faster than in the one-electron case. In addition, the thinnest ring shows an oscillation component with a phase difference of π producing local conductance minima at integer number of flux quanta [100]. This phase shift arises from the interference of the electron density scattered along the transport channels and

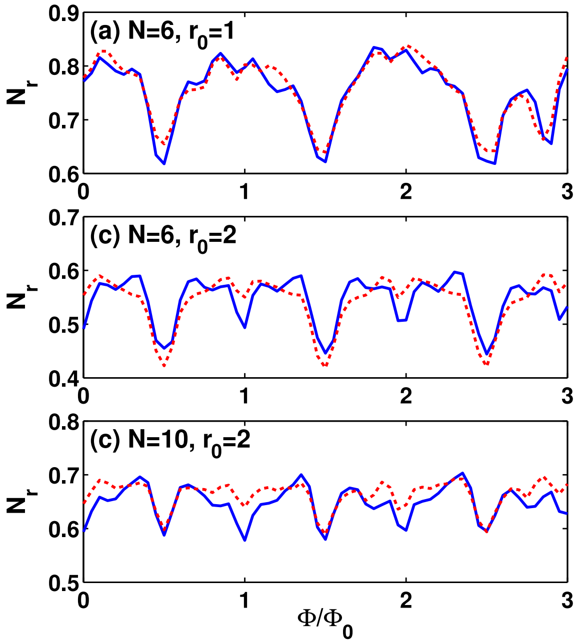

Figure 3.4: Transferred relative number of electrons for different QRs with (dashed lines) and without (solid lines) interactions at $t = 3.0$. The width of the QRs is the same $a = 0.5$ for different radii. (a) $N = 6$ and $r_0 = 1$. (b) $N = 6$ and $r_0 = 2$. (c) $N = 10$ and $r_0 = 2$.

the unscattered electron density.

To test the effect of the electron-electron interactions we repeat the conductance calculations for six and ten electrons with and without interactions. The many-electron conductance with two different ring diameters is plotted in Fig. 3.4. Increasing the ring diameter makes the system relatively more strongly interacting as the Coulomb energy scales as r^{-1}, whilst the kinetic energy scales as r^{-2}. For $r = 1$, the interacting and noninteracting cases produce similar magnetoconductance. Doubling the radius to $r = 2$ induces some changes in the overal shape of the magnetoconductance curve, but the qualitative difference between the noninteracting and interacting cases remains small, i.e., the AB oscillations are preserved with and without interactions. Increasing the electron number N decreases the AB oscillation amplitude as shown in six- and ten-electron QRs in Figs. 3.4(b) and (c). In addition, the π-shifted component (see the previous section) is reduced when the interactions are made stronger or when the electron number is increased.

Our results indicate the the visibility of the AB oscillations is sensitive to both the width of the QR as well as to the number of electrons confined in the ring. We conclude that only the few highest energy states along a narrow path are occupied in a successful AB transport measurement.

3.2 Transport in Aharonov-Bohm interferometers

3.2.1 Background

Combining quantum Hall effect (QHE) with the Aharonov-Bohm (AB) effect makes it possible to design interferometry devices that can be controlled by the external magnetic field alone. Recent low-temperature measurements in Fabry-Pérot [101–105] and Mach-Zehnder [106, 107] interferometers have utilized the QHE via current channel formation in high magnetic fields and the AB effect to control the electron dynamics. The magnetotransport studies in quantum Hall (QH) systems are partly motivated by the possibility of topological quantum computing [108] as well as interesting fractional statistics in two-dimensional systems [103]. In QH interferometers the electron paths depend on the magnetic field in contrast to original AB experiments. This interesting feature and the effect of the channel widths are not taken into account in the common single-particle edge-state approach [109].

The aim of our study [110, 111] is to model the formation of the current-carrying incompressible strips for a given heterostructure and apply time-dependent density-functional theory to examine its transport characteristics. This allows us to determine the effect of the incompressible strip width and position to electron transport in addition to the magnetic field.

3.2.2 Device and electrostatics

Our study proceeds in two parts. First, we follow the method presented in Sec. 2.5 and apply the 3D Poisson equation and the Thomas-Fermi approximation to the sample geometry obtained from Goldman *et al.* [101] (see Fig. 3.5). Now we can obtain the electron density and potential distribution under QH conditions. The semiclassical approximation used in this part is valid because the number of electrons is very large (of the order of 10^3).

The resulting filling factor (density) distribution is shown in Fig. 3.5. We can see that the distance between the incompressible strips, i.e., the region where $\nu = 2$ decreases, while the strip width becomes larger as the magnetic field is increased. Since the AB effect requires tunneling between the current channels, it is expected that the AB oscillations are weaker or not present at all when the magnetic field is smaller and the electrons remain in the incoming channel. The visibility of the AB oscillations is also reduced when the magnetic field is increased too much. This occurs because the incompressible strips overlap and all electrons are transfered to the other channel. Clear AB interference requires even splitting of the current between the two channels.

According to the single-electron picture, the current flows through chiral edge states, i.e., the direction of the current is different at the opposite sides of the sample. This is true for the equilibrium transport, but if an external current is imposed, as it is done in experiments, the situation changes. The external current leads to a position-dependent electrochemical potential and the formation of the potential differences with the same slope to the opposite sides of the sample. The potential drops at the incompressible strips, which confines the currents flowing to the same direction in those regions [58, 60]. This picture is used in the transport calculations presented in the following section.

3.2.3 Transport model

Next, we construct a model potential describing the positions of the current-carrying incompressible strips. The cross section of the model potential is approximately Gaussian, $v_{\mathrm{ext,cross}}(x) \sim \exp(-x^2/a^2)$, where x is a coordinate perpendicular to the channel and a controls the channel width. The Gaussian cross section is used because it is a good approximation for the parabolic magnetic confinement at the bottom of the channel, while it allows "leaking" of the electron flow between the channels. In addition to the variable channel width, the distance between the current channels can also be changed in a way that the potential minima at the encountering points are separated by a distance $d \in [0, 1]$. A schematic image describing the model potential and showing the encountering points is presented in Fig. 3.5.

The initial state is calculated by selecting a small portion of the current channel from the lower-left part of the potential and using it for the many-electron ground-state calculation. The resulting wave packet, which is used to model the excess electron density on top of the Fermi background, is accelerated through the system using a linear potential along the channel at the lower-left side of the potential. We continue the time propagation of the system until the backscattering effects from the upper left and right corners of our finite simulation box are observed. This makes sure that the current direction is correct during the time-propagation.

The conductance as a function of the magnetic flux Φ through the loop formed by the current channels and encounter points (see Fig. 3.5), the channel separation d, and the channel width w is estimated by the transmission factor $N_r(\Phi, d, w, t)$. It is calculated by integrating the electron density at top right corner of the device (see Sec. 2.10).

In contrast to a real interferometer, the channel width and separation are considered here to be independent of the magnetic field. This is justified by noting that according to the electrostatic calculation presented in the previous section, notable changes in the spatial distribution of incompressible strips can be seen when the magnetic field change is about $\Delta B \sim 0.1...0.4$ T (see Fig. 3.5). In typical samples in the micrometer scale this corresponds about change of 100...400 flux quanta in magnetic flux. Since we consider changes within only three flux quanta, the shape of the channels can be assumed to be approximately constant. Here Φ is the magnetic flux added to the background flux which induces the incompressible current channels.

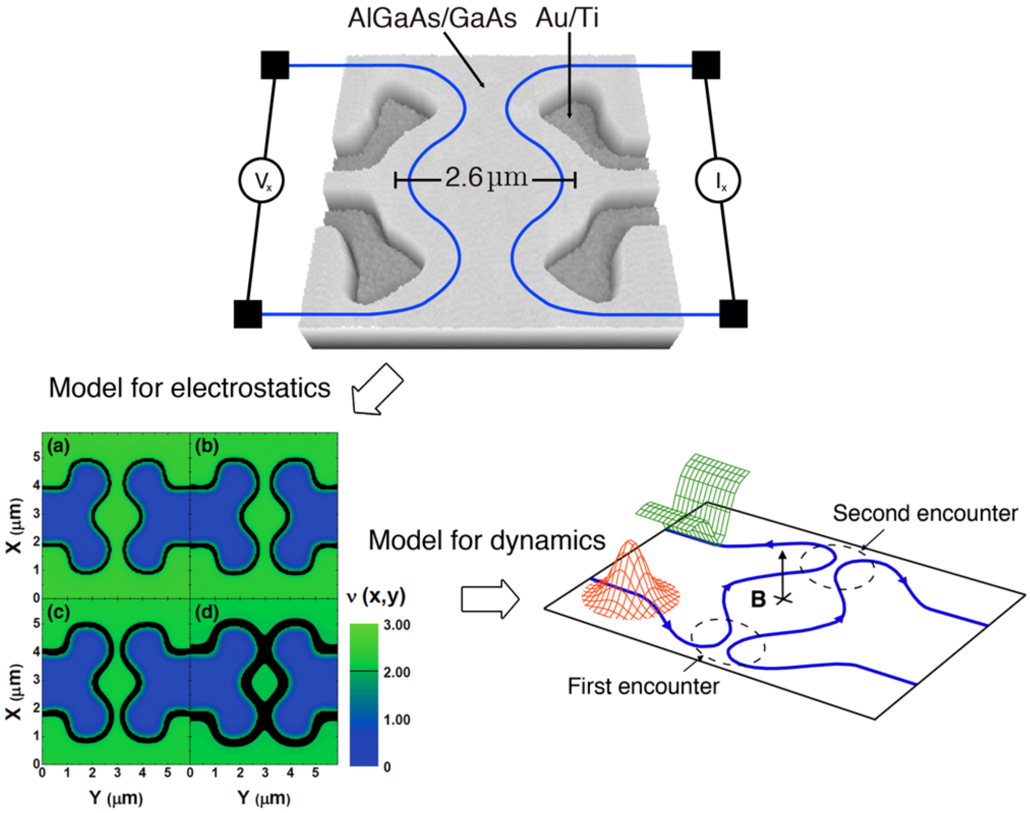

Figure 3.5: Top: Atomic force microscope image of the experimental device by Camino *et al.* The device consists of AlGaAs/GaAs heterojunction with Au/Ti gate structure. Reprinted figure with permission from [101]. Copyright (2005) by the American Physical Society. Lower-left: Spatial distribution of the incompressible strips (black, $\nu = 2$) calculated with different magnetic fields. (a) $B = 7.6$ T, (b) $B = 8.0$ T, (c) $B = 8.4$ T, (d) $B = 8.8$ T. Lower-right: Schematic image of the transport setup. The upper mesh represents the cross sction of the channel along the blue thick lines. The lower mesh shows the initial state for the time-propagation. The magnetic flux is calculated for the perpendicular uniform magnetic field and the area restricted by the channel minima and encounter points. With kind permission from Springer Science and Business Media, originally published in European Physical Journal B **86**, 155 (2013).

3.2.4 Transport results

We start by examining the effect of the channel width and separation in the one-electron case. The resulting AB oscillation amplitude is visualized in Fig. 3.6, where a clear region of the maximum amplitude can be seen. The maximum appears when the splitting of the electron wave packet is *equal* after the first encounter point. If the distance between the channels is too small, more than a half of the density tunnels to the right-hand channel in the first encounter point and the amplitude is smaller. Similarly, if the channel separation is too large, less than a half of the density is tunneled and the amplitude is smaller. The channel width can be used to modulate this effect, e.g., if the channel separation is too large, the channels need to be wider. The secondary maximum occurs when a part of the wave packet is reflected back and forth across the first encounter point resulting in an even distribution between the channels. We note that the amplitude of the secondary maximum is partly affected by the undesired back-scattering at the first encounter point.

Next, we examine the transport of a single-electron wave packet with a non-zero magnetic field. The evolution of the electron density with $\Phi/\Phi_0 = 0$ and $\Phi/\Phi_0 = 0.5$ is visualized with density snapshots in Fig. 3.7. The distribution of the electron density is similar during the first three frames. The difference

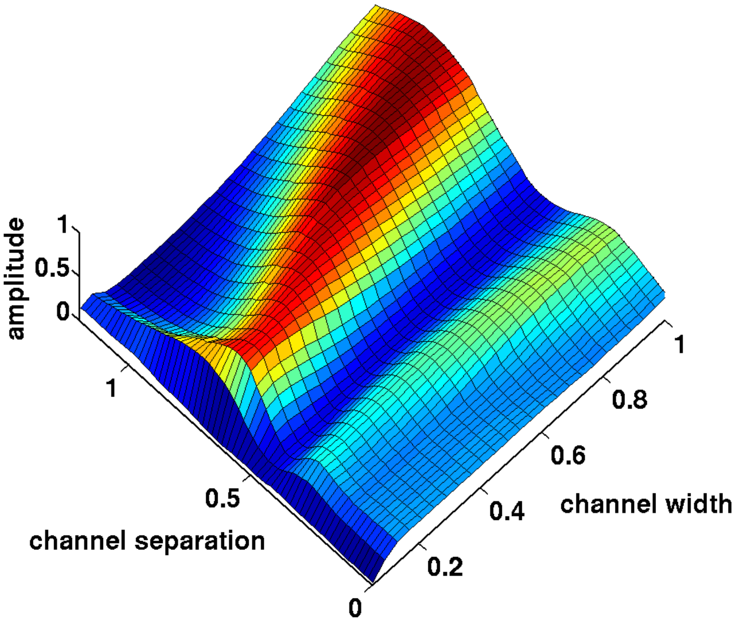

Figure 3.6: Estimated AB oscillation amplitude as a function of the channel width and separation in zero magnetic field. The AB oscillation amplitude has a maximum (red) when the wave packet distribution is even in the first encounter point.

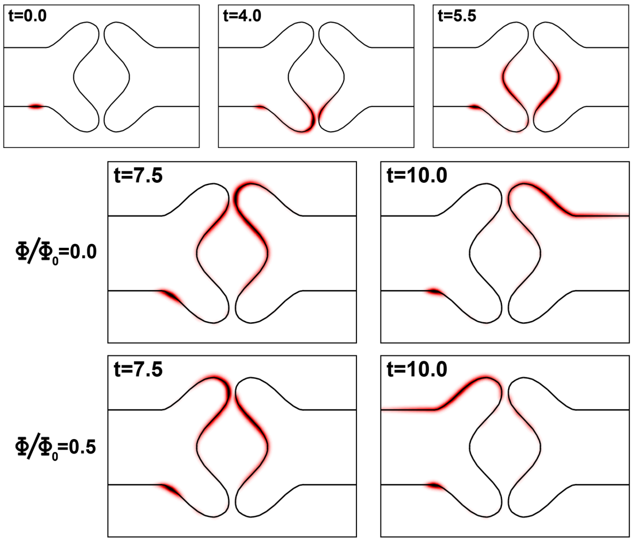

Figure 3.7: Snapshots of the electron density in a model for the AB interferometer. The two lowermost rows correspond to zero flux and half a flux quantum, respectively.

becomes drastic after the second encounter point when zero flux (second row) leads to complete transport to the top-right corner while the half-flux quantum case (third row) directs the electron density to the upper-left side. Thus, we are able to tune the transport direction by utilizing the AB effect.

We start examining the effect of interactions by simulating the transmission of a two-electron wave packet through the interferometer device with channel width $a = 0.3$ (see Figs. 2 and 3 of Ref. [111]). We can find distinctive AB oscillations with all channel separations d for noninteracting electrons. Turning on the interactions preserves the AB oscillation period but induces a small phase shift that depends on the channel separation. We also see that the visibility of the AB oscillation strongly depends on the channel separation with and without interactions, and the maximum visibility is always found at $d \approx 0.4$. A detailed examination of the electron densities reveals that the maximum visibility is obtained when the partition is equal at the first encounter point, just like in the one-electron case. Consequently, the interference at the second point of the encounter is as complete as possible. The relative amount of the correlation energy E_c depends on the density parameter r_s defined as the area occupied by one electron,

$$\pi r_s^2 n = 1 \ \rightarrow \ r_s = \frac{1}{\sqrt{\pi n}}. \tag{3.2}$$

For GaAs samples in $\sim$ 10...50 nm size scale with $N = 1...10$ electrons the correlation energy is much smaller than the exchange energy, i.e., $|E_c| << |E_x|$ [9]. Hence, the observed similarity between the EXX and LDA results can be regarded as the validation of the LDA calculation in this case.

For ten electrons the effect of the interactions becomes more pronounced (see Figs. 4 and 5 of Ref. [111]). The maximum amplitude is still obtained with the similar channel separation $d \approx 0.4$ as in the two-electron case. The optimal visibility of AB oscillations is not reduced as a function of the electron number N, but the oscillation amplitude is reduced by interactions when the channel distance is not optimal. This is shown in Fig. 3.8, where the maximum amplitude in the whole range $\Phi/\Phi_0 = 0...3$ is plotted as a function of the interchannel distance. We find that the noninteracting ten-electron system has approximately twice the oscillation visibility compared to the interacting system at $d = 0.6$.

The phase shift found in the two-electron simulation is more pronounced when the number of electrons is increased. In the ten-electron case the EXX is unstable and is replaced by a more stable Hartree approximation, where the exchange and correlation are omitted. The results in the high-visibility regime are similar and generally the deviations are modest. Overall, the high-visibility region is not affected by the electron-electron interactions and therefore, we expect the AB oscillations to be always visible if the location of the incompressible strips – controlled by the magnetic field – is optimal for the partitioning. However, the phase shift becomes visible only at the price of suppressing the visibility. The summary of the AB oscillation visibility and the phase shift for two, six, and ten electrons is presented in Fig. 3.9.

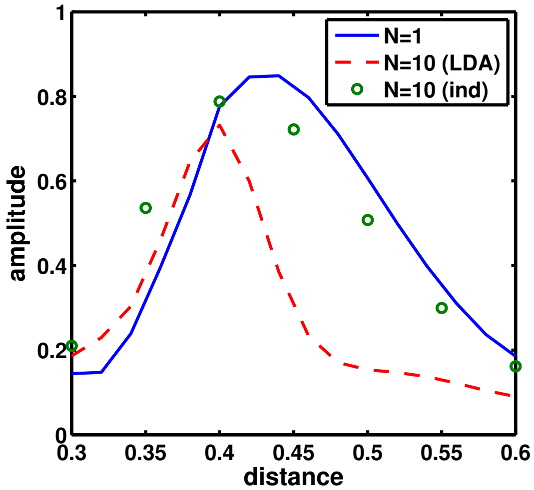

Figure 3.8: Maximum amplitude of the AB oscillation (from minimum to maximum transmission) in the range $\Phi/\Phi_0 = 0...3$ in the case of $N = 1$ (solid line), $N = 10$ calulated with the adiabatic LDA (dashed line) and without interactions (circles). With kind permission from Springer Science and Business Media, originally published in European Physical Journal B **86**, 155 (2013).

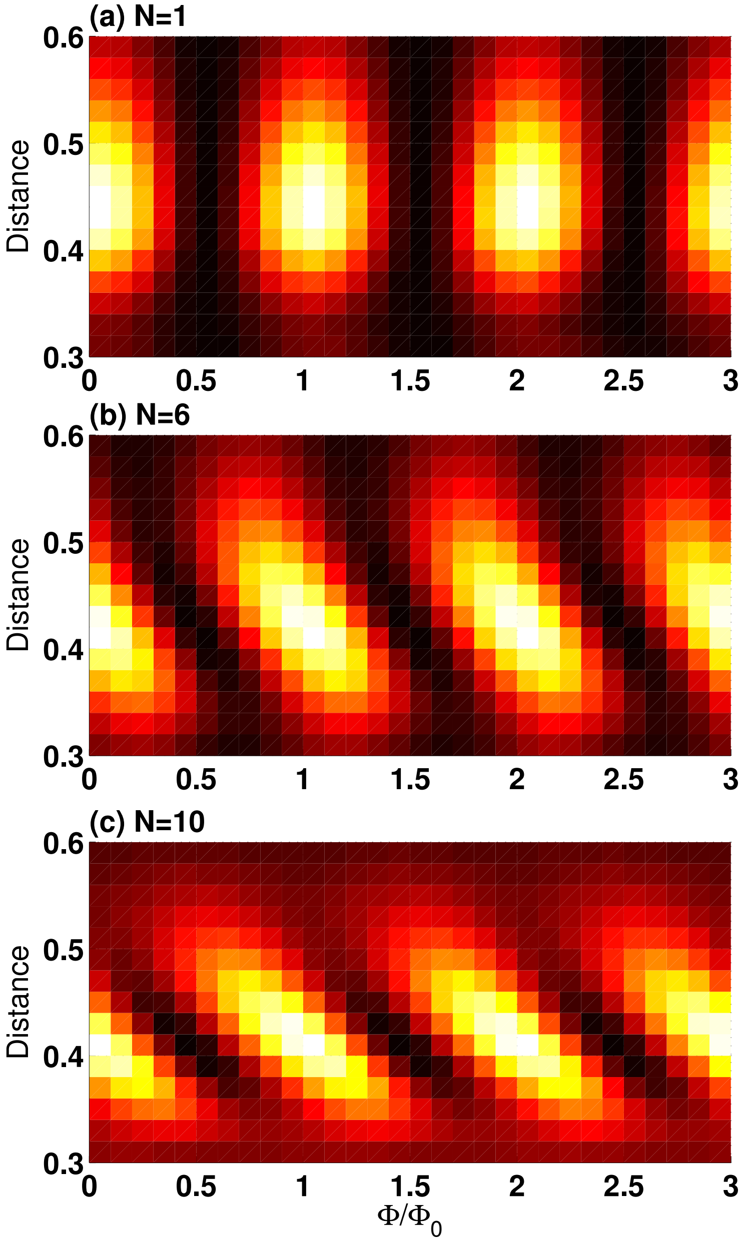

Figure 3.9: Aharonov-Bohm oscillations (color scale) for one-, six-, and ten-electron systems, respectively. Clear phase shifts can be seen in many-electron systems treated here within adiabatic LDA. With kind permission from Springer Science and Business Media, originally published in European Physical Journal B **86**, 155 (2013).

3.3 Fractal dynamics in chaotic quantum transport

3.3.1 Background

In the final part of the thesis, we consider transport characteristics of a stadium-shaped quantum billiard. A stadium billiard is a standard example of a classically chaotic system [69]. When a perpendicular magnetic field is applied, its phase space is mixed, i.e., it contains chaotic and non-chaotic trajectories.

Interestingly, stadium-shaped quantum dots have been experimentally realized already since 1990's [112]. The experimental setup consists of the 2D electron gas (2DEG) in a semiconductor heterostructure, where the quantum dot itself is defined by the use of metallic gates [71, 112–114]. The magnetoconductance of a stadium quantum dot displays fluctuations that have fractal scaling properties. Systems having a mixed phase space display probability distributions $P(A) \sim A^{-\gamma}$ for areas A enclosed by trajectories. It was proposed by Ketzmerick [115], that a power law for the area distribution leads to fractal characteristics in the conductance.

Dynamics in chaotic cavities has been studied with a broad selection of theoretical methods. There are semiclassical trajectory-based studies [115, 116] and tight-binding calculations [117, 118] of conductance, just to name a few. The aim of this study is to determine fractal scaling properties of magnetoconductance in an open quantum stadium billiard treated with a full 2D model in real space and time. We numerically solve the time-dependent Schrödinger equation on a grid for the desired geometry, which allows more realistic modeling of quantum transport compared to the semiclassical treatment and the tight-binding calculations.

Conventionally, transport problems such as this can be handled by calculating the coupling matrix between the eigenstates of the quantum dot and the leads. The major challenge in this method is to solve the 2D eigenvalue problem efficiently for the chaotic quantum dot in a static magnetic field. Novel methods in solving the single-particle Schrödinger equation in magnetic fields [119] may extend the previously described conventional transport scheme accordingly. In any case, here we use the same scheme as in previous chapters to estimate the conductance.

3.3.2 Model

We construct a model for a two-terminal stadium quantum dot similar to the experimental setup in Ref. [71]. The potential (see Fig. 3.10) has hard walls and consists of a stadium with radius $r = 1.0$ and width $d = 0.7$, input and output leads of width $w = 0.56$, and a linear potential that is used to emulate the source-drain voltage. A small part of the input lead is used to calculate the initial state for the time-propagation, and the transmission factor $T(\Phi, t)$ is calculated by

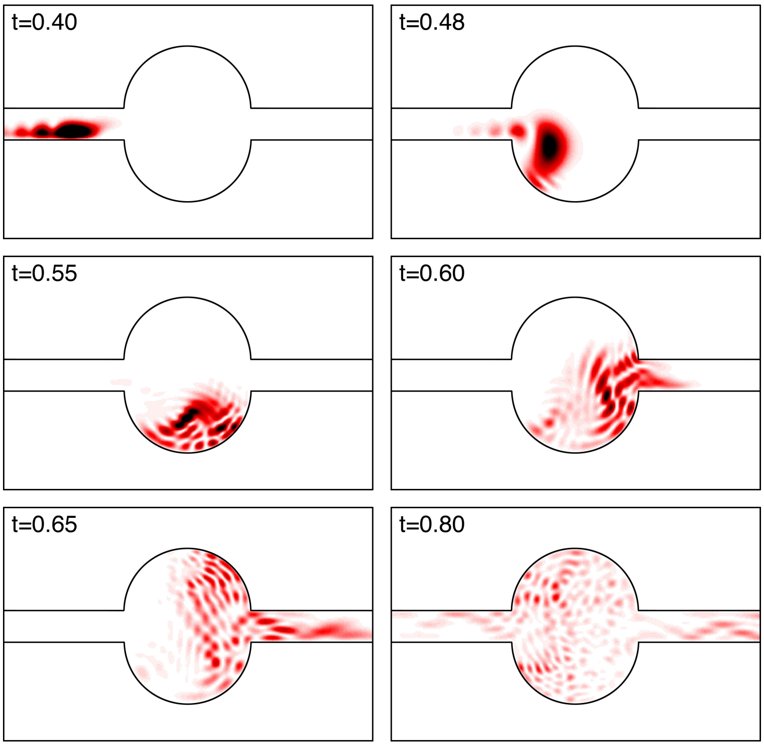

Figure 3.10: Snapshots of the electron density in the model stadium system (see the text) during a transport simulation with the magnetic flux $\Phi/\Phi_0 = 20$. The input and output leads extend further to the left and right.

integrating the electron density in the output lead (see Sec. 2.10). The fractal characteristics of the magnetoconductance is analyzed with the variation method (VM) and the detrended fluctuation analysis (DFA) introduced in Sec. 2.7.

3.3.3 Transport results

An example of electron dynamics in the stadium is shown in Fig. 3.10. Approximately a half of the electron density is transmitted through and the other half is either backscattered to the input lead or confined in the stadium. The momentum of the wave packet determines the size of the density bumps during the scattering process, where the higher eigenstates are probed with higher momentum. The initial momentum of the wave packet is chosen in such a way that the used grid spacing is sufficient to describe the dynamics inside the quantum dot.

The transmission factor as a function of the magnetic flux and time is presented in Fig. 3.11. A complex magnetoconductance pattern is formed after time $t = 1.0$. We are not able to reach the equilibrium current due to the finite system size and must discard the results where undesired backscattering effects become visible. One of such effects can be seen in Fig. 3.11 at zero flux and

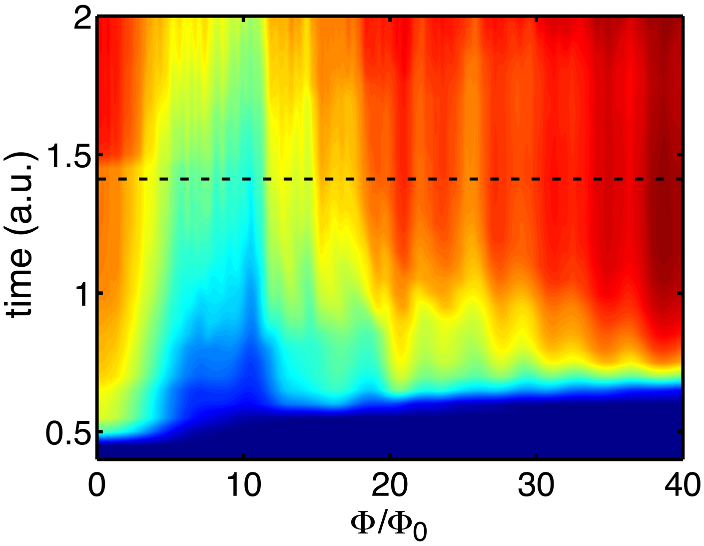

Figure 3.11: Transmission factor as a function of time and magnetic flux through the stadium quantum dot. The curve in Fig. 3.12 represents a cut along the dashed line, which turns out to be a fractal.

time $t = 1.5$, where the step is a consequence of electron backscattering between the quantum dot and the accelerating linear potential. A cross section of the transmission factor at $t = 1.4$ is shown in Fig. 3.12. The general trend of the transmission builds up as follows: First, the increasing magnetic field depopulates trajectories directly coupling the input and output leads. After reaching the minimum, the transmission factor starts to rise due to an increased number of skipping orbits which propagate along the device boundaries. Finer details in the magnetoconductance are formed due to the chaotic behavior of the system through the whole range of the magnetic flux considered here.

Next, fractal properties of the obtained conductance are analyzed with the VM and a slightly modified version of DFA. When studying conductance fluctuations, the DFA exponent α needs to be related to the fractal dimension D. It is known that $D = 2 - \gamma/2$ with $\langle(\Delta G)^2\rangle \propto (\Delta B)^\gamma$ [71, 115] where the latter is exactly Step (4) of DFA squared (see section 2.7.2). We therefore omit Step (1), identify $\alpha = \gamma$, and get

$$D = 2 - \frac{\alpha}{2} \tag{3.3}$$

for the fractal dimension.

We apply the quadratic DFA ($m = 2$) to our data in Fig. 3.12. The fitting of the data at $t = 1.4$ is shown in inset. The obtained result $\alpha = 1.46$ is in good qualitative agreement with the experimental result $\gamma = \alpha = 1.38$ of Sachrajda *et al.* [71]. The experimental fractal dimension is $D = 1.25$, which agrees very well with our DFA ($D = 1.27$) and VM ($D = 1.32$) results.

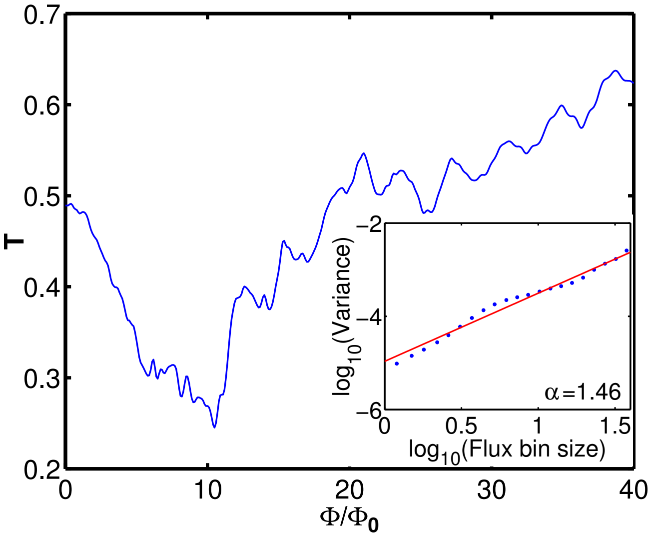

Figure 3.12: Transmission factor as a function of the magnetic field at $t = 1.4$. The inset shows the scaling exponent $\alpha = 1.46$ obtained from the DFA analysis.

The fractal dimensions obtained with the DFA and the VM are shown as a function of time in Fig. 3.13(a). The fitting errors $\eta = 1 - R^2$, where R is the pearson product-moment correlation coefficient of log-log data, are shown in Fig. 3.13(b). The error parameter η measures the fit quality such that $\eta = 0$ corresponds to exact linear behavior. A visual inspection of Fig. 3.11 suggests that clear signatures of a fractal structure develop only after $t = 1.0$. This can be seen in the convergence of the fractal dimension D and the minimization of the fitting error in Fig. 3.13. At times larger than $t = 1.4$ the fitting error increases due to backscattering effects resulting from the finite simulation box (see above). In this way we are able to determine the range of validity in our scheme to calculate the fractal dimension.

Finally, we point out that various experiments in chaotic quantum-dot systems have produced qualitatively similar fractal dimensions [120, 121]. In addition, it has been recently found out that the disorder has a considerable role in the magnetoconductance of modulation-doped quantum dots. The magnetoconductance can be modified by thermal cycling which changes the position of the donor atoms, i.e., the source of the disorder potential. On the other hand, the thermal cycling yields reproducible properties in electrostatically doped samples [114].

The transport model presented in this thesis is straightforward to be adjusted for different geometries and potential shapes. Future prospects include more realistic modeling of quantum dot boundaries by varying their softness [71, 115, 121, 122], by testing different shapes for the contacts, and by the inclusion of arbitrary impurity potentials [114].

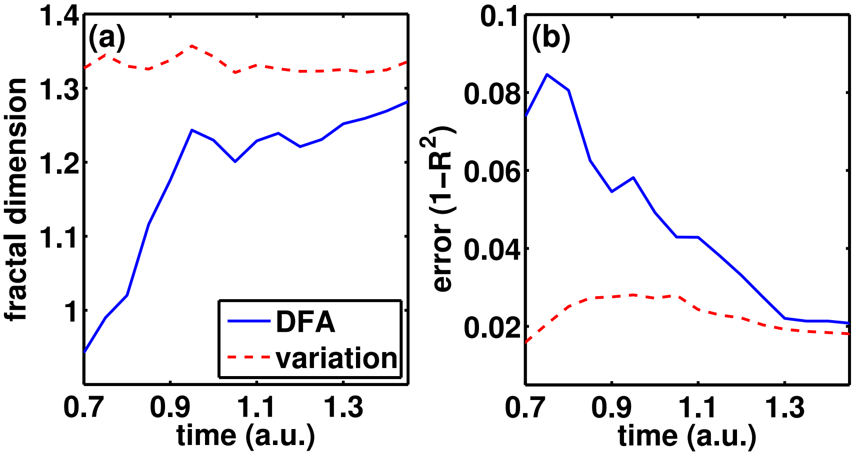

Figure 3.13: (a) Fractal dimension D calculated from DFA with the relation $D = 2 - \alpha/2$ and from the VM during the time propagation. Note that the fractal structure is developed only at $t \gtrsim 1$. (b) Time development of the error in the fitting procedure at $t = 0.7...1.4$ (see text).

Chapter 4

Summary

In this thesis, electronic transport properties of 2D quantum dots in perpendicular magnetic fields have been examined by numerically solving the time-dependent Schrödinger equation on a real-space grid and the time-dependent density functional theory (TDDFT). With our scheme we can simultaneously examine real-time dynamics as well as the role of electron-electron interactions and the 2D character of the system with realistic conduction channels.

The first study (Article I) focuses on investigating the Aharonov-Bohm (AB) effect in many-electron quantum rings. We have modeled the electron transport by considering the discharge of a one-terminal quantum ring and by calculating the relative number of escaped electrons. AB oscillations with a period $\Phi_0/n = h/(en)$ are found, where $n = 1$ and $n > 1$ correspond to regular AB oscillations and oscillations that arise when the electron density travels multiple times around the quantum ring, respectively. Increasing the width of conduction channel dramatically decreases the visibility of the AB oscillations, i.e., the oscillation amplitude. On the other hand, we have found that the electron-electron interactions have a relatively small effect on the oscillation visibility. Our simulations suggest that the transport is dominated by a few electrons traveling in a thin conduction channel near the Fermi level whenever AB oscillations are visible in quantum-ring experiments.

The second study (Articles II and III) considers quantum transport in AB interferometers. We have solved the electron density and the spatial distribution of the incompressible strips in the experimental geometry. Next, the obtained distribution of the current-carrying incompressible strips has been used as a base to build a model potential for the electron transport simulation. We have found that the transport across the device is highly dependent on the channel width and the interchannel distance. The transmission through the device displays clear AB oscillations whose visibility is maximised when the electron density distribution is even between the current carrying channels. In addition, the magnetic field can be used to switch the current between the two outgoing leads. Increasing the number of noninteracting electrons does not affect the relative transport characteristics but adding interactions induces a phase shift in AB oscillation as a function of the interchannel distance. The strength of the phase-shift is proportional to the number of electrons, while the maximum visibility is not affected by the interactions.

Finally, the fractal characteristics of a transport through a classically chaotic quantum dot has been studied (Article IV). We have propagated a single-electron wave packet through the stadium-shaped quantum dot and obtained a complete picture of the magnetoconductance. The magnetoconductance has been analyzed with the use of the detrended fluctuation analysis, a widely-used method in time-series analysis, and its results have been compared to the variation analysis. Both methods produce similar results and show clear signs of fractal scaling. Excellent qualitative agreement with previous experiments in a similar system has been obtained.

The transport scheme introduced in this thesis can be easily applied to different geometries in one, two, and three dimensions. One of the possible future applications is the inclusion of the arbitrary disorder potential in the system of interest to examine the central role of impurities in quantum transport. These studies could clarify the ongoing discussion on the characteristics of quantum transport in semiconductor structures, especially with respect to diffusive vs. ballistic features.

References

[1] P. Moller. *Electric Fish.* BioScience **41**, 794 (1991).

[2] J. J. Thomson. *Cathode Rays.* Philosophical Magazine Series 5 **44**, 293 (1987).

[3] M. Planck. *Über das Gesetz der Energieverteilung im Normalspektrum.* Annalen Der Physik **4**, 553 (1901).

[4] L. de Broglie. *Recherches sur la théorie des quanta.* Ann. Phys. (Paris) **3**, 22 (1925).

[5] E. Schrödinger. *An undulatory theory of the mechanics of atoms and molecules.* Phys. Rev. **29**, 1049 (1926).

[6] W. Heisenberg. *Über den anschaulichen Inhalt der quantentheoretischen Kinematik und Mechanik.* Zeitschrift für Physik **43**, 172 (1927).

[7] C. Davisson and L. H. Germer. *Diffraction of electrons by a crystal of nickel.* Phys. Rev. **30**, 705 (1927).

[8] G. E. Uhlenbeck and S. Goudsmit. *Ersetzung der Hypothese vom unmechanischen Zwang durch eine Forderung bezüglich des inneren Verhaltens jedes einzelnen Elektrons.* Die Naturwissenschaften **13**, 953 (1925).

[9] G. G. Giuliani and G. Vignale. *Quantum Theory of the Electron Liquid.* Cambridge University Press (2005). ISBN 978-0-521-52796-4.

[10] E. Fermi. *Sulla quantizzazione del gas perfetto monoatomico.* Rend. Lincei **3**, 145 (1926).

[11] P. A. M. Dirac. *The Quantum Theory of the Electron.* Proc. R. Soc. Lond. A **117**, 610 (1928).

[12] H. K. Onnes. *The resistance of pure mercury at helium temperatures.* Commun. Phys. Lab. Univ. Leiden **12**, 120 (1911).

[13] J. Bardeen, L. N. Cooper, and J. R. Schrieffer. *Microscopic Theory of Superconductivity.* Phys. Rev. **106**, 162 (1957).

[14] G. E. Moore. *Cramming more components onto integrated circuits.* Electronics Magazine **April**, 4 (1965).

[15] N. M. R. Peres. *Colloquium: The transport properties of graphene: And introduction.* Rev. Mod. Phys. **82**, 2673 (2010).

[16] M. Z. Hasan and C. L. Kane. *Colloquium: Topological insulators.* Rev. Mod. Phys. **82**, 3045 (2010).

[17] K. von Klitzing, G. Dorda, and M. Pepper. *New Method for High-Accuracy Determination of the Fine-Structure Constant Based on Quantized Hall Resistance.* Phys. Rev. Lett. **45**, 494 (1980).

[18] D. C. Tsui, H. L. Stormer, and A. C. Gossard. *Two-Dimensional Magnetotransport in the Extreme Quantum Limit.* Phys. Rev. Lett. **48**, 1559 (1982).

[19] R. B. Laughlin. *Anomalous Quantum Hall Effect: An Incompressible Quantum Fluid with Fractionally Charged Excitations.* Phys. Rev. Lett **50**, 1395 (1983).

[20] S. M. Reimann and M. Manninen. *Electronic structure of quantum dots.* Rev. Mod. Phys. **74**, 1283 (2002).

[21] Y. Alhassid. *The statistical theory of quantum dots.* Rev. Mod. Phys. **72**, 895 (2000).

[22] P. Hohenberg and W. Kohn. *Inhomogeneous Electron Gas.* Phys. Rev. **136**, B864 (1964).

[23] W. Kohn and L. J. Sham. *Self-Consistent Equations Including Exchange and Correlation Effects.* Phys. Rev. **140**, A1133 (1965).

[24] K. Burke. *Perspective on density functional theory.* J. Chem. Phys. **136**, 150901 (2012).

[25] J. P. Perdew. *Accurate Density Functional for the Energy: Real-Space Cutoff of the Gradient Expansion for the Exchange Hole.* Phys. Rev. Lett. **55**, 1665 (1985).

[26] J. P. Perdew, K. Burke, and Y. Wang. *Generalized gradient approximation for the exchange-correlation hole of many-electron system.* Phys. Rev. B **54**, 16533 (1996).

[27] J. P. Perdew, K. Burke, and M. Ernzerhof. *Generalized Gradient Approximation Made Simple.* Phys. Rev. Lett. **77**, 3865 (1996).

[28] A. D. Becke. *Density-functional exchange-energy approximation with correct asymptotic behavior.* Phys. Rev. A **38**, 3098 (1988).

[29] A. D. Becke. *Density-functional thermochemistry. III. The role of exact exchange.* J. Chem. Phys **98**, 5648 (1993).

[30] C. Lee, W. Yang, and R. G. Parr. *Development of the Colle-Salvetti correlation-energy formula into a functional of the electron density.* Phys. Rev. B **37**, 785 (1988).

[31] P. J. Stephens, F. J. Devlin, and C. F. Chabalowski. *Ab Initio Calculation of Vibrational Absorption and Circular Dichroism Spectra Using Density Functional Force Fields.* J. Phys. Chem. **98**, 11623 (1994).

[32] J. P. Perdew, S. Kurth, A. Zupan, and P. Blaha. *Accurate Density Functional with Correct Formal Properties: A Step Beyond the Generalized Gradient Approximation.* Phys. Rev. Lett. **82**, 2544 (1999).

[33] J. P. Perdew, A. Ruzsinszky, G. I. Csonka, L. A. Constantin, and J. Sun. *Workhorse Semilocal Density Functional for Condensed Matter Physics and Quantum Chemistry.* Phys. Rev. Lett. **103**, 026403 (2009).

[34] A. Görling. *Orbital- and state-dependent functionals in density-functional theory.* J. Chem. Phys. **123**, 062203 (2005).

[35] S. Kümmel and L. Kronik. *Orbital-dependent density functionals: Theory and applications.* Rev. Mod. Phys. **80**, 3 (2008).

[36] C. Attaccalite, S. Moroni, P. Gori-Giorgi, and G. B. Bachelet. *Correlation Energy and Spin Polarization in the 2D Electron Gas.* Phys. Rev. Lett. **88**, 256601 (2002).

[37] U. von Barth. *Basic Density-Functional Theory - an Overview.* Physica Scripta **T109**, 9 (2004).

[38] A. Harju, H. Saarikoski, and E. Räsänen. *Half-Integer Filling Factor States in Quantum Dots.* Phys. Rev. Lett. **96**, 126805 (2006).

[39] E. Räsänen, H. Saarikoski, A. Harju, M. Ciorga, and A. S. Sachrajda. *Spin droplets in confined quantum Hall systems.* Phys. Rev. B **77**, 041302(R) (2008).

[40] N. Helbig, S. Kurth, S. Pittalis, E. Räsänen, and E. K. U. Gross. *Exchange-correlation orbital functionals in current-density functional theory: Application to a quantum dot in magnetic fields.* Phys. Rev. B **77**, 245106 (2008).

[41] K. Burke, J. Werschnik, and E. K. U. Gross. *Time-dependent density functional theory: Past, present, and future.* J. Chem. Phys. **123**, 062206 (2005).

[42] E. Runge and E. K. U. Gross. *Density-Functional Theory for Time-Dependent Systems.* Phys. Rev. Lett. **52**, 997 (1984).

[43] C. A. Ullrich. *Time-Dependent Density-Functional Theory, Concepts and Applications.* Oxford University Press (2012).

[44] R. van Leeuwen. *Mapping from Densities to Potentials in Time-Dependent Density-Functional Theory.* Phys. Rev. Lett. **82**, 3863 (1999).

[45] M. Ruggenthaler and R. van Leeuwen. *Global fixed-point proof of time-dependent density-functional theory.* Europhys. Lett. **95**, 13001 (2011).

[46] G. Vignale and M. Rasolt. *Density-Functional Theory in Strong Magnetic Fields.* Phys. Rev. Lett. **59**, 2360 (1987).

[47] Y. Aharonov and D. Bohm. *Significance of Electromagnetic Potentials in the Quantum Theory.* Phys. Rev. **115**, 485 (1959).

[48] Y. Aharonov and D. Bohm. *Further Considerations on Electromagnetic Potentials in the Quantum Theory.* Phys. Rev. **123**, 1511 (1961).

[49] R. G. Chambers. *Shift of an electron interference pattern by enclosed magnetic flux.* Phys. Rev. Lett. **5**, 3 (1960).

[50] J. M. Alberty. *Aharonov-Bohm Interferometry with Quantum Dots as Phase Shifters : Simulations.* In Proceedings of the COMSOL Multiphysics User's Conference (2005).

[51] *Kosmos: Livets fysik.* v. 63. Swedish Science Press (1986). ISBN 9789186344351.

[52] B. Jeckelmann and B. Jeanneret. *The Quantum Hall Effect as an Electrical Resistance Standard.* Séminaire Poincaré **2**, 39 (2004).

[53] M. Oestreich and W. W. Rühle. *Temperature Dependence of the Electron Landé g Factor in GaAs.* Phys. Rev. Lett. **74**, 2315 (1995).

[54] D. B. Chklovskii, B. I. Shklovskii, and L. I. Glazman. *Electrostatics of edge channels.* Phys. Rev. B **46**, 4026 (1992).

[55] R. B. Laughlin. *Quantized Hall conductivity in two dimensions.* Phys. Rev. B **23**, 5632 (1981).

[56] B. Kramer, S. Kettemann, and T. Ohtsuki. *Localization in the quantum Hall regime.* Physica E **20**, 172 (2003).

[57] B. I. Halperin. *Quantized Hall conductance, current-carrying edge states, and the existence of extended states in a two-dimensional disordered potential.* Phys. Rev. B **25**, 2185 (1982).

[58] K. Guven and R. R. Gerhardts. *Self-consistent local equilibrium model for density profile and distribution of dissipative currents in a Hall bar under strong magnetic fields.* Phys. Rev. B **67**, 115327 (2003).

[59] A. Siddiki and R. R. Gerhardts. *Incompressible strips in dissipative Hall bars as origin of quantized Hall plateaus.* Phys. Rev. B **70**, 195335 (2004).

[60] E. Ahlswede, P. Weitz, J. Weis, K. von Klitzing, and K. Eberl. *Hall potential profiles in the quantum Hall regime measured by a scanning force microscope.* Physica B **298**, 562 (2001).

[61] E. Ahlswede, J. Weis, K. von Klitzing, and K. Eberl. *Hall potential distribution in the quantum Hall regime in the vicinity of a potential probe contact.* Physica E **12**, 165 (2002).

[62] E. N. Lorenz. *Deterministic Nonperiodic Flow.* Journal of The Atmospheric Sciences **20**, 130 (1963).

[63] L. M. Pecora and T. L. Carroll. *Synchronization in Chaotic Systems.* Phys. Rev. Lett. **64**, 821 (1990).

[64] A. Garfinkel, M. L. Spano, W. L. Ditto, and J. Weiss. *Controlling Cardiac Chaos.* Science **257**, 1230 (1992).

[65] S. J. Schiff, K. Jerger, D. H. Duong, T. Chang, M. L. Spano, and W. L. Ditto. *Controlling Chaos in the Brain.* Nature **370**, 615 (1994).

[66] S. H. Strogatz. *Nonlinear Dynamics and Chaos.* Perseus Books Publishing (2000).

[67] O. Bohigas, M. J. Giannoni, and C. Schmit. *Characterization of Chaotic Quantum Spectra and Universality of Level Fluctuation Laws.* Phys. Rev. Lett. **52**, 1 (1984).

[68] M. L. Mehta. *Random Matrices.* Academic Press (1991). ISBN 0-12-488051-7.

[69] H.-J. Stöckmann. *Quantum Chaos, an introduction.* Cambridge University Press (2006).

[70] M. S. Santhanam, J. N. Bandyopadhyay, and D. Angom. *Quantum spectrum as a time series: Fluctuation measures.* Phys. Rev. E **73**, 015201(R) (2006).

[71] A. S. Sachrajda, R. Ketzmerick, C. Gould, Y. Feng, P. J. Kelly, A. Delage, and Z. Wasilewski. *Fractal Conductance Fluctuations in a Soft-Wall Stadium and a Sinai Billiard.* Phys. Rev. Lett. **80**, 1948 (1998).

[72] C.-K. Peng, S. Havlin, H. E. Stanley, and A. L. Goldberger. *Quantification of scaling exponents and crossover phenomena in nonstationary heartbeat time series.* Chaos **5**, 82 (1995).

[73] A. L. Goldberger, L. A. N. Amaral, J. M. Hausdorff, P. C. Ivanov, C.-K. Peng, and H. E. Stanley. *Fractal dynamics in physiology: Alterations with disease and aging.* PNAS **99**, 2466 (2002).

[74] R. F. Voss and J. Clarke. *'1/f noise' in music and speech.* Nature **258**, 317 (1975).

[75] K. J. Hsü and A. J. Hsü. *Fractal geometry of music.* Proc. Natl. Acad. Sci. **87**, 938 (1990).

[76] H. Hennig, R. Fleischmann, Y. H. A. Fredebohm, J. Nagler, A. Witt, F. Theis, and T. Geisel. *The Nature and Perception of Fluctuations in Human Musical Rhythms.* PLoS ONE **6**, e26457 (2011).

[77] H. Hennig, R. Fleischmann, and T. Geisel. *Musical rhythms: The science of being slightly off.* Physics Today **65**, 64 (2012).

[78] J. M. Hausdorff, C. K. Peng, Z. Ladin, J. Y. Wei, and A. L. Goldberger. *Is walking a random walk? Evidence for long-range correlations in stride interval of human gait.* J Appl Physiol **78**, 349 (1995).

[79] B. Dubuc, J. F. Quiniou, C. Roques-Carmes, C. Tricot, and S. W. Zucker. *Evaluating the fractal dimension of profiles.* Phys. Rev. A **39**, 1500 (1989).

[80] C.-K. Peng, S. V. Buldyrev, S. Havlin, M. Simons, H. E. Stanley, and A. L. Goldberger. *Mosaic organization of DNA nucleotides.* Phys. Rev. E **49**, 1685 (1994).

[81] B. Pilgram and D. T. Kaplan. *A comparison of estimators for* $1/f$ *noise.* Physica D **114**, 108 (1997).

[82] S. Elliott. *The Physics and Chemistry of Solids.* John Wiley & Sons Ltd (2006).

[83] M. A. L. Marques, A. Castro, G. F. Bertsch, and A. Rubio. *octopus: a first-principles tool for excited electron-ion dynamics.* Comput. Phys. Commun. **151**, 60 (2003).

[84] A. Castro, H. Appel, M. Oliveira, C. A. Rozzi, X. Andrade, F. Lorenzen, M. A. L. Marques, E. K. U. Gross, and A. Rubio. *octopus: a tool for the application of time-dependent density functional theory.* Phys. Stat. Sol. B **243**, 2465 (2006).

[85] X. Andrade, J. Alberdi-Rodriguez, D. A. Strubbe, M. J. T. Oliveira, F. Nogueira, A. Castro, J. Muguerza, A. Arruabarrena, S. G. Louie, A. Aspuru-Guzik, A. Rubio, and M. A. L. Marques. *Time-dependent density-functional theory in massively parallel computer architectures: the octopus project.* J. Phys.: Cond. Matt. **24**, 233202 (2012).

[86] A. Castro, M. A. L. Marques, and A. Rubio. *Propagators for the time-dependent Kohn–Sham equations.* J. Chem. Phys. **121**, 3425 (2004).

[87] M. Di Ventra. *Electrical Transport in Nanoscale Systems.* Cambridge University Press (2008). ISBN 978-0-521-89634-4.

[88] R. A. Webb, S. Washburn, C. P. Umbach, and R. B. Laibowitz. *Observation of h/e Aharonov-Bohm Oscillations in Normal-Metal Rings.* Phys. Rev. Lett. **54**, 2696 (1985).

[89] G. Timp, A. M. Chang, J. E. Cunningham, T. Y. Chang, P. Mankiewich, R. Behringer, and R. E. Howard. *Observation of the Aharonov-Bohm Effect for* $\omega_c\tau > 1$. Phys. Rev. Lett. **58**, 2814 (1987).

[90] Y. Gefen, Y. Imry, and M. Y. Azbel. *Quantum Oscillations and the Aharonov-Bohm Effect for Parallel Resistors.* Phys. Rev. Lett. **52**, 129 (1984).

[91] M. Büttiker, Y. Imry, and M. Y. Azbel. *Quantum oscillations in one-dimensional normal-metal rings.* Phys. Rev. A **30**, 1982 (1984).

[92] P. Vasilopoulos, O. Kálmán, F. M. Peeters, and M. G. Benedict. *Aharonov-Bohm oscillations in a mesoscopic ring with asymmetric arm-dependent injection.* Phys. Rev. B **75**, 035304 (2007).

[93] A. Fuhrer, S. Lüscher, T. Ihn, T. Heinzel, K. Ensslin, W. Wegscheider, and M. Bichler. *Energy spectra of quantum rings.* Nature **413**, 822 (2001).

[94] D.-I. Chang, G. L. Khym, K. Kang, Y. Chung, H.-J. Lee, M. Seo, M. Heiblum, D. Mahalu, and V. Umansky. *Quantum mechanical complementarity probed in a closed-loop Aharonov-Bohm interferometer.* Nat. Phys. **4**, 205 (2008).

[95] K. N. Pichugin and A. F. Sadreev. *Aharanov-Bohm(sic) oscillations of conductance in two-dimensional rings.* Phys. Rev. B **56**, 9662 (1997).

[96] J. Wurm, M. Wimmer, H. U. Baranger, and K. Richter. *Graphene rings in magnetic fields: Aharonov-Bohm effect and valley splitting.* Semicond. Sci. Technol. **25**, 034003 (2009).

[97] B. Szafran and F. M. Peeters. *Time-dependent simulations of electron transport through a quantum ring: Effect of the Lorentz force.* Phys. Rev. B **72**, 165301 (2005).

[98] A. Chaves, G. A. Farias, F. M. Peeters, and B. Szafran. *Wave packet dynamics in semiconductor quantum rings of finite width.* Phys. Rev. B **80**, 125331 (2009).

[99] C. Kreisbeck, T. Kramer, S. S. Buchholz, S. F. Fischer, U. Kunze, D. Reuter, and D. Wieck. *Phase shifts and phase π jumps in four-terminal waveguide Aharonov-Bohm interferometers.* Phys. Rev. B **82**, 165329 (2010).

[100] V. Kotimäki and E. Räsänen. *Aharonov-Bohm effect in many-electron quantum rings.* Phys. Rev. B **81**, 245316 (2010).

[101] F. E. Camino, W. Zhou, and V. J. Goldman. *Aharonov-Bohm electron interferometer in the integer quantum Hall regime.* Phys. Rev. B **72**, 155313 (2005).

[102] F. E. Camino, W. Zhou, and V. J. Goldman. *Quantum transport in electron Fabry-Perot interferometers.* Phys. Rev. B **76**, 155305 (2007).

[103] F. E. Camino, W. Zhou, and V. J. Goldman. *Aharonov-Bohm Superperiod in a Laughlin Quasiparticle Interferometer.* Phys. Rev. Lett. **95**, 246802 (2005).

[104] D. T. McClure, Y. Zhang, B. Rosenow, E. M. Levenson-Falk, C. M. Marcus, L. N. Pfeiffer, and K. W. West. *Edge-State Velocity and Coherence in a Quantum Hall Fabry-Pérot Interferometer.* Phys. Rev. Lett. **103**, 206806 (2009).

[105] Y. Zhang, D. T. McClure, E. M. Levenson-Falk, C. M. Marcus, L. N. Pfeiffer, and K. W. West. *Distinct signatures for Coulomb blockade and Aharonov-Bohm interference in electronic Fabry-Pérot interferometers.* Phys. Rev. B **79**, 241304(R) (2009).

[106] P. Roulleau, F. Portier, D. C. Glattli, P. Roche, A. Cavanna, G. Faini, U. Gennser, and D. Mailly. *Finite bias visibility of the electronic Mach-Zehnder interferometer.* Phys. Rev. B **2007**, 161309(R) (2007).

[107] L. V. Litvin, H.-P. Tranitz, W. Wegscheider, and C. Strunk. *Decoherence and single electron charging in an electronic Mach-Zehnder interferometer.* Phys. Rev. B **75**, 033315 (2007).

[108] S. Das Sarma, M. Freedman, and C. Nayak. *Topologically Protected Qubits from a Possible Non-Abelian Fractional Quantum Hall State.* Phys. Rev. Lett. **94**, 166802 (2005).

[109] M. Büttiker. *Four-Terminal Phase-Coherent Conductance.* Phys. Rev. Lett. **57**, 1761 (1986).

[110] V. Kotimäki, E. Cicek, A. Siddiki, and E. Räsänen. *Time-dependent transport in Aharonov-Bohm interferometers.* New J. Phys. **14**, 053024 (2012).

[111] A. Salman, V. Kotimäki, A. Siddiki, and E. Räsänen. *Many-electron transport in Aharonov-Bohm interferometers: A time-dependent density-functional study.* Eur. Phys. J. B **86**, 155 (2013).

[112] C. M. Marcus, A. J. Rimberg, R. M. Westervelt, P. F. Hopkins, and A. C. Gossard. *Conductance Fluctuations and Chaotic Scattering in Ballistic Microstructures.* Phys. Rev. Lett. **69**, 506 (1992).

[113] A. P. Micolich, R. P. Taylor, A. G. Davies, J. P. Bird, R. Newbury, T. M. Fromhold, A. Ehlert, H. Linke, L. D. Macks, W. R. Tribe, E. H. Linfield, D. A. Ritchie, J. Cooper, Y. Aoyagi, and P. B. Wilkinson. *Evolution of Fractal Patterns during a Classical-Quantum Transition.* Phys. Rev. Lett. **87**, 036802 (2001).

[114] A. M. See, I. Pilgrim, B. C. Scannell, R. D. Montgomery, O. Klochan, A. M. Burke, M. Aagesen, and P. E. Lindelof. *Impact of Small-Angle Scattering on Ballistic Transport in Quantum Dots.* Phys. Rev. Lett. **108**, 196807 (2012).

[115] R. Ketzmerick. *Fractal conductance fluctuations in generic chaotic cavities.* Phys. Rev. B **54**, 10841 (1996).

[116] S. Heusler, S. Müller, P. Braun, and F. Haake. *Semiclassical Theory of Chaotic Conductors.* Phys. Rev. Lett. **96**, 066804 (2006).

[117] E. Louis and J. A. Vergés. *Self-similar magnetoconductance fluctuations in quantum dots.* Phys. Rev. B **61**, 13014 (2000).

[118] Y. Takagaki and K. H. Ploog. *Numerical simulation of fractal conductance fluctuations in soft-wall quantum cavities.* Phys. Rev. B **61**, 4457 (2000).

[119] P. J. J. Luukko and R. Räsänen. *Imaginary time propagation code for large-scale two-dimensional eigenvalue problems in magnetic fields.* Comput. Phys. Commun. **184**, 769 (2013).

[120] A. P. Micolich, R. P. Taylor, T. P. Martin, R. Newbury, T. M. Fromhold, A. G. Davies, H. Linke, W. R. Tribe, L. D. Macks, C. G. Smith, E. H. Linfield, and D. A. Ritchie. *Three key questions on fractal conductance fluctuations: Dynamics, quantization, and coherence.* Phys. Rev. B **70**, 085302 (2004).

[121] C. A. Marlow, R. P. Taylor, T. P. Martin, B. C. Scannell, H. Linke, M. S. Fairbanks, G. D. R. Hall, I. Shorubalko, L. Samuelson, T. M. Fromhold, C. V. Brown, B. Hackens, S. Faniel, C. Gustin, V. Bayot, X. Wallart,

S. Bollaert, and A. Cappy. *Unified model of fractal conductance fluctuations for diffusive and ballistic semiconductor devices.* Phys. Rev. B **73**, 195318 (2006).

[122] A. P. Micolich, R. P. Taylor, A. G. Davies, T. M. Fromhold, and H. Linke. *Dependence of fractal conductance fluctuations on soft-wall profile in a double-layer semiconductor billiard.* Appl. Phys. Lett. **80**, 4381 (2002).